

Title	Study on Extreme Ultraviolet Sensitization Mechanism of Resist Polymers Having Onium Salt as Side Chain
Author(s)	小室, 嘉崇
Citation	大阪大学, 2015, 博士論文
Version Type	VoR
URL	<a href="https://doi.org/10.18910/52143">https://doi.org/10.18910/52143</a>
rights	
Note	

*Osaka University Knowledge Archive : OUKA*

<https://ir.library.osaka-u.ac.jp/>

Osaka University

# Doctoral Dissertation

Study on Extreme Ultraviolet Sensitization Mechanism of Resist

Polymers Having Onium Salt as Side Chain

(オニウム塩を側鎖に持つレジスト高分子の極端紫外光に  
対する感光機構に関する研究)

Yoshitaka Komuro

January 2015

Department of Applied Chemistry

Graduate School of Engineering,

Osaka University



## **Preface**

The studies presented here have been carried out under the direction of Professor Takahiro Kozawa from April 2012 to March 2015 at Department of Applied Chemistry, Graduate School of Engineering, Osaka University.

The object of the thesis is to clarify the extreme ultraviolet sensitization mechanism of polymers having onium salt as side chain.

YOSHITAKA Komuro

**Department of Applied Chemistry**

**Graduate School of Engineering**

**Osaka University**

**Suita, Osaka**

**Japan**

**January 2015**

## **Contents**

<b>General Introduction</b>	<b>1</b>
-----------------------------	----------

### **Chapter 1**

#### **Electron and Hole Transfer in Anion-Bound Chemically Amplified Resists Used in Extreme Ultraviolet Lithography**

1.1. Introduction	15
1.2. Experiment	17
1.2.1. Material	17
1.2.2. Nanosecond electron pulse radiolysis – kinetics	18
1.2.3. HPLC measurement condition	19
1.3. Result and discussion	19
1.3.1. Nanosecond pulse-radiolysis of cyclohexanone	19
1.3.2. Nanosecond pulse-radiolysis of anion-bound polymer	21
1.4. Summary	29

### **Chapter 2**

#### **Acid generation mechanism in anion-bound chemically amplified resists used for extreme ultraviolet lithography**

2.1. Introduction	34
2.2. Experiment	34
2.2.1 Material	34
2.2.2. EUV radiolysis – acid yield	35
2.2.3. $\gamma$ radiolysis – product analysis	36

2.3. Result and discussion	38
2.4. Summary	46

### **Chapter 3**

#### **Modeling and simulation of acid generation in anion-bound chemically amplified resists used for extreme ultraviolet lithography**

3.1. Introduction	51
3.2. Experiment	52
3.2.1. X-ray diffractometer – film density	52
3.2.2 Dielectric constants	52
3.3. Simulation model	53
3.4. Results and discussion	60
3.5. Summary	71
<b>Conclusion</b>	<b>74</b>
<b>List of publications</b>	<b>76</b>
<b>Acknowledgments</b>	<b>76</b>

## **General Introduction**

The development of electronic devices such as computers and smartphones was accomplished by the miniaturization of semiconductor devices. The miniaturization of semiconductor devices has enabled the improvement of components per chip and speed of processing. In addition, the cost reduction has been achieved by reducing the wafer area per component chip. A transistor was invented by John Bardeen and Walter Brattain at AT&T Bell Laboratory in 1948.<sup>1,2)</sup> Since their invention and the following invention of the integrated circuit (IC) made by Jack Killby and Robert Noyce in 1959, the transistor has been highly integrated and developed. The early integrated circuit (IC) was called SSI (Small Scale Integration) and small number of transistors were integrated. Today, ULSI (Ultra large scale integration) with  $10^9$  transistors (1 billion units) is being developed. Gordon E. Moore who is a co-founder of Intel Corporation predicted that the integration density of transistors in an IC will increase 4-fold in three years (Moore's Law). The degree of integration of transistors has followed the Moore's Law for more than 30 years since his prediction. The essence of the law is to coordinate the development directions of device manufactures, equipment manufacturers, process material manufactures and chemical manufactures. The physical limits of miniaturization have been often discussed since twenty years ago. The apparent physical limits have been broken by the technological innovations.



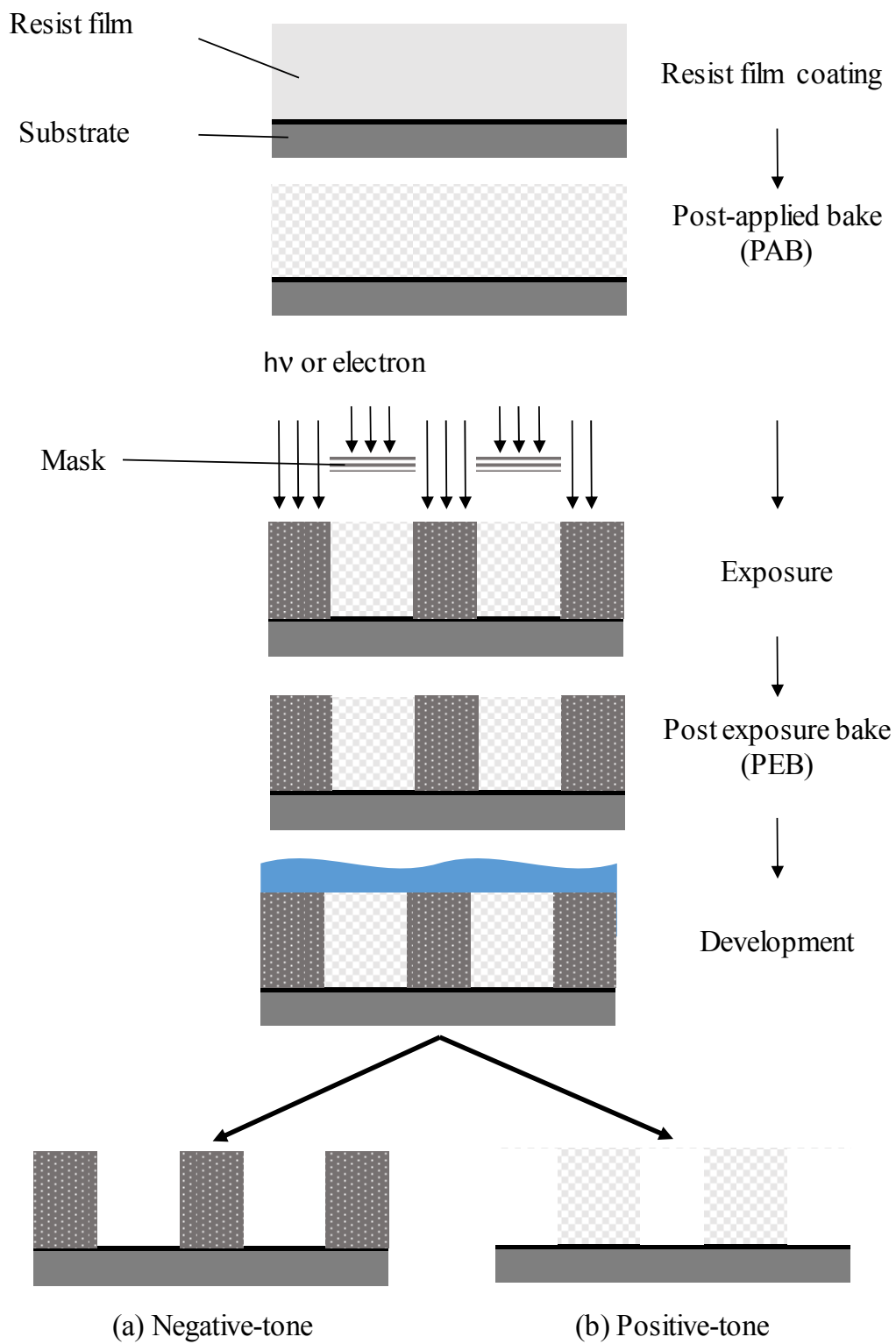


Figure 1. The lithographic process (a) negative-tone resist and (b) positive-tone resist.

A technology for the miniaturization and integration is called lithography. In the late 18th century, the lithography was developed and used for printing not only texts but also art. Currently, the lithography is the process of transferring patterns in a photomask to a radiation-sensitive material layer called a resist. Figure 1 shows traditional lithographic processes. First, a resist is coated on the substrate such as a silicon wafer by using spin coater. Next, the resist film is exposed to radiation such as photons and electrons through a mask. The chemical property of exposed resist is changed through cross-linking reaction, main chain degradation, or polarity change. The exposed region is dissolved in the developer (positive-tone resist). A pattern is formed utilizing the difference in solubility for the developer between the exposed and unexposed area. The limit of the lithography resolution is expressed by the Rayleigh Equation,

$$R = k_1 \times \lambda / NA \quad (1)$$

Here,  $R$ ,  $\lambda$ ,  $NA$ , and  $k_1$  are the resolution, the exposure wavelength, the numerical aperture of the lens, and a process factor, respectively.

The resolution of lithography has been improved mainly by decreasing the exposure wavelength. Figure 2 shows the trends in the feature size and production year of DRAM and major exposure wavelength.<sup>3)</sup> The exposure wavelength has been changed from i-line (365 nm) of ultra-high pressure mercury lamp to KrF (248 nm) and ArF (193 nm)

of excimer lasers. The wavelength has become 20~30% shorter in the 5-7 year cycle. The fabrication of sub-10 nm features is required for the next generation lithography. Extreme ultraviolet (EUV) lithography as an extension of photolithography is capable of resolving sub-10 nm half pitch,<sup>4)</sup> and the leading candidate that succeeds the current 193 nm lithography.

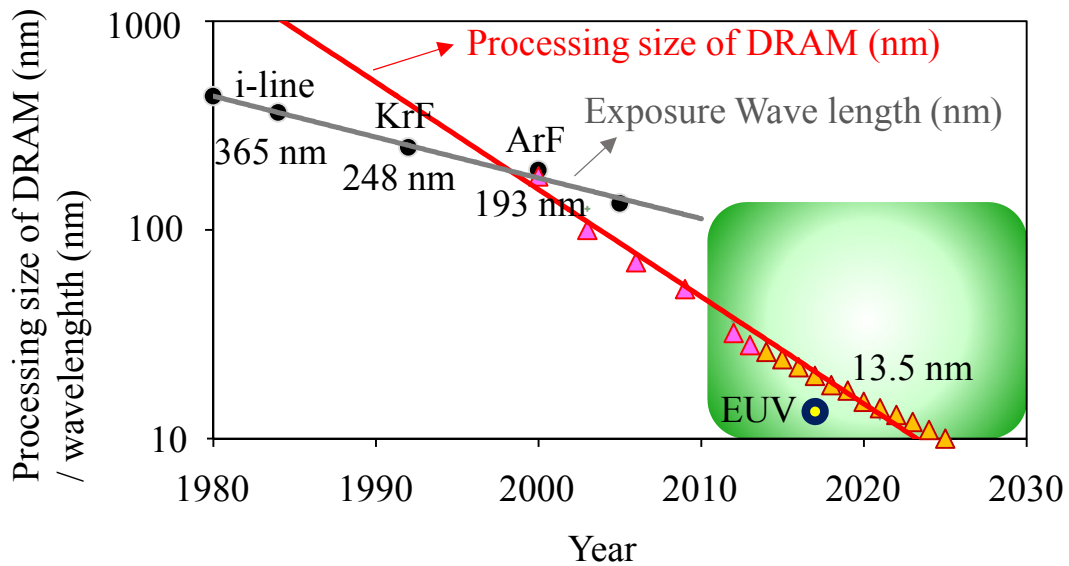


Figure 2. Relationship between processing size and exposure wavelength.

In 1982, Ito et al. proposed a chemically amplified resist (CAR).<sup>5)</sup> The CAR generally contains a photo acid generator (PAG) that produces acid upon exposure to a radiation. The reaction of generated acids with acid-labile protecting groups of the polymer changes the polarity of the polymer, as shown in Fig. 3.

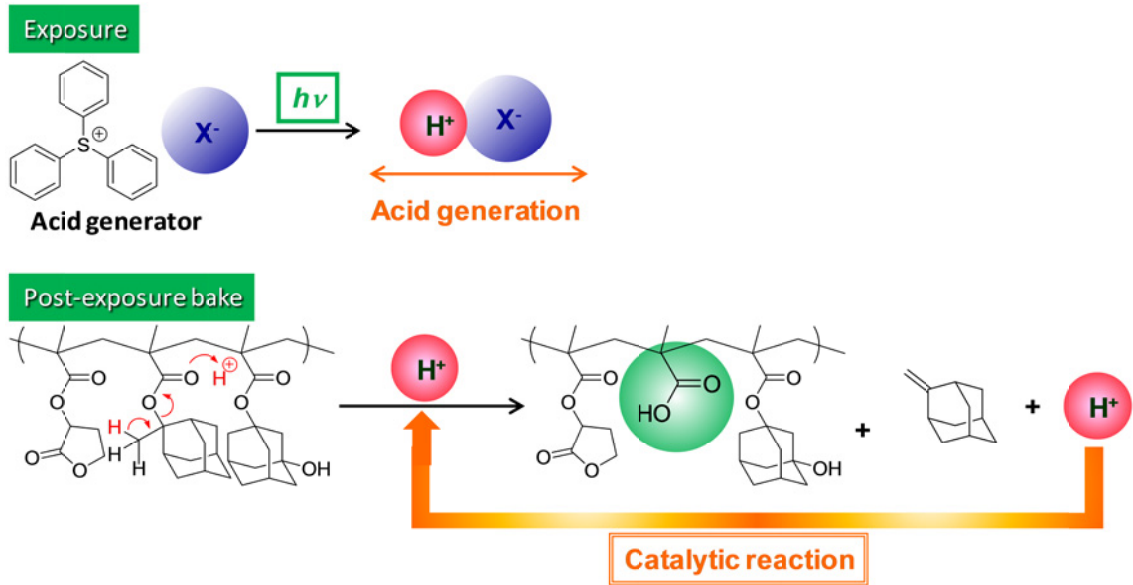


Figure 3. Resist chemistry in the most popular positive-tone chemically amplified resist.

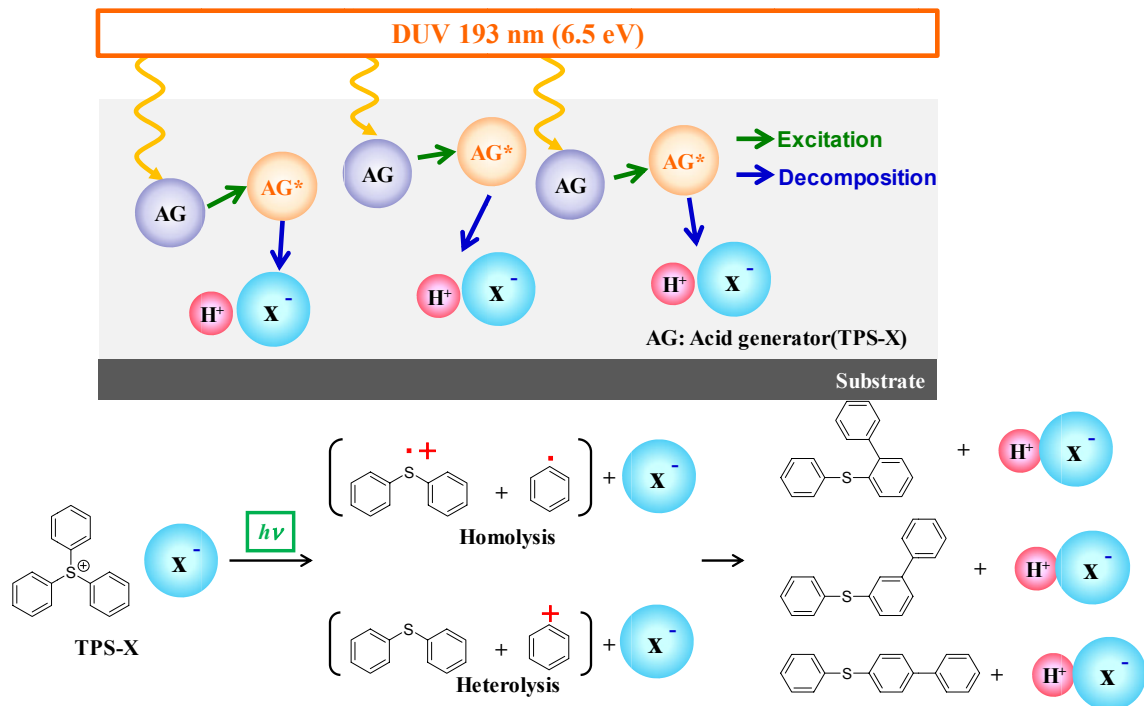


Figure 4. Acid generation mechanisms induced by DUV photons.

The generated acids proceed a large number of reactions as a catalyst upon heating. Therefore, even if the quantum yield of the generated acids is 1 or less, the quantum yield of deprotection exceeds. The photosensitization mechanisms of next generation EUV lithography are known to differ from those of conventional optical lithography such as KrF and ArF lithography. Because the photon energies of conventional KrF and ArF excimer lasers are less than the ionization potential of resist materials, the sensitization mechanism of the conventional optical lithography is the direct electronic excitation of acid generators by incident photons (Fig. 4).<sup>6,7)</sup> On the other hand, the energy of EUV (92.5 eV) exceeds the ionization potential of resist materials. The energy of radiation is mostly deposited on polymer matrices via ionization. When EUV photons enter resist materials, polymer radical cations and photoelectrons are generated through ionization. The photoelectrons generated further induce ionization until their energy is lost sufficiently. The low-energy electrons then react with acid generators. Through their reaction with low-energy electrons, acid generators dissociate into counteranions of Brønsted acids and other products. Protons are generated through the deprotonation of polymer radical cations (Figure 5).<sup>8,9)</sup>

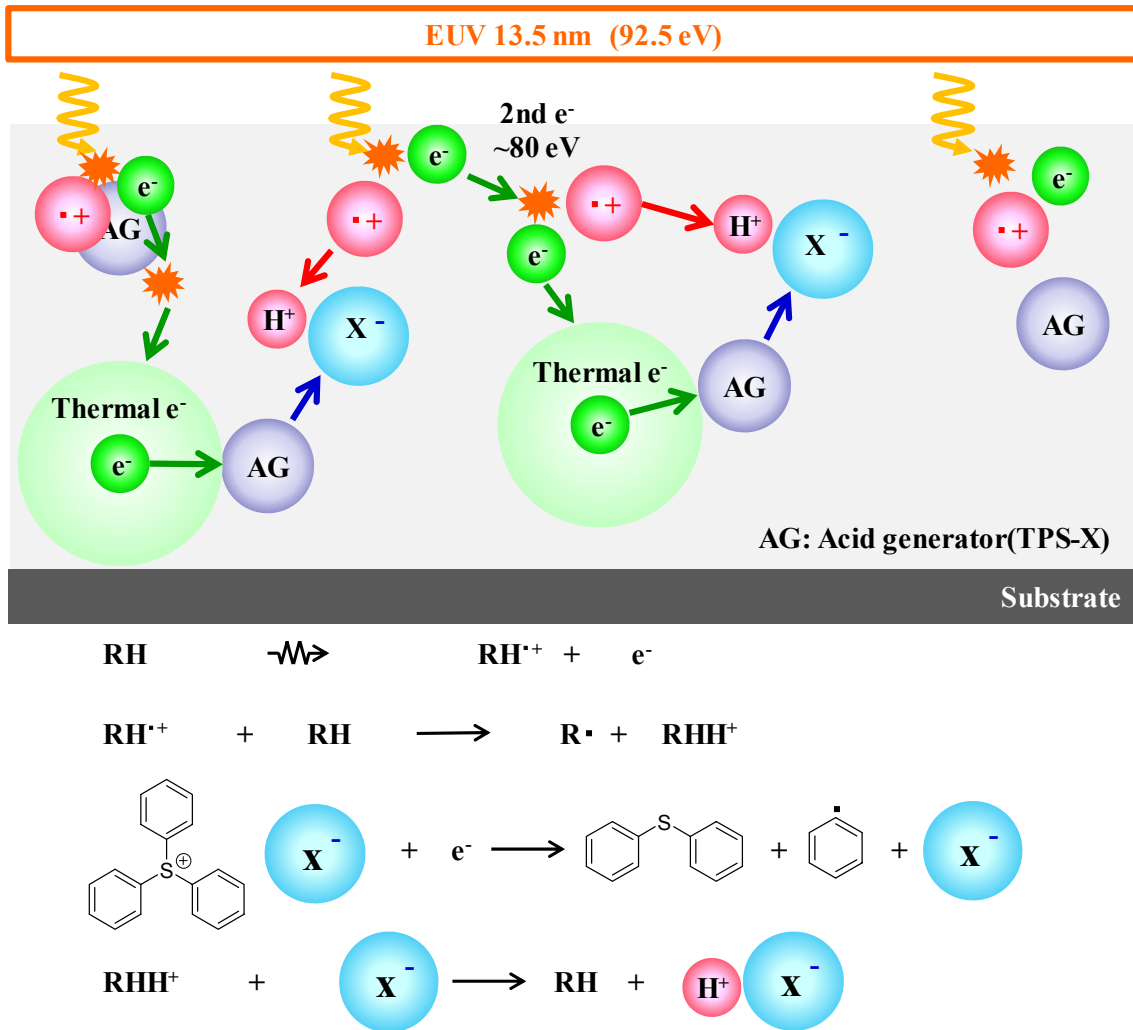


Figure 5. Acid generation mechanisms induced by EUV photons.

For the resist materials used for the lithography, not only the resolution, but also the sensitivity and line-width roughness (LWR) are important factors from the viewpoint of yield and throughput of semiconductor device manufacturing. The degradation of LWR causes the disconnection or deterioration of electric property. However, these requirements (resolution, LWR, and sensitivity) are in a trade-off relationship (RLS

trade-off). The trade-off relationships between resolution, LWR and sensitivity are the most serious problem in the development of resist materials. To solve such trade-off problems, novel chemically amplified resist materials must be developed. It has been speculated that the main cause of reaction blur in a chemically amplified resist is acid diffusion.<sup>10-12)</sup> The increase in acid generator concentration and the suppression of the subsequent acid diffusion is one way to simultaneously improve resolution and LWR.<sup>13-18)</sup> On the other hand, the feature size is shrinking so markedly that the uniformity of acid generator distribution in resist matrices is becoming a serious problem. The phase separation between resist components has also been suggested.<sup>19-21)</sup> The best way to solve the above-mentioned problems is the incorporation of acid generators into polymers typically via covalent bonds. Particularly, the incorporation of the anion part of acid generators into polymers (anion-bound polymer, ABP) is expected to improve LWR and achieve a high resolution by reducing acid diffusion length. Also, the anion-bound polymer is expected to improve the uniformity of the acid generator distribution in resist matrices. Many attempts to incorporate ionic and nonionic acid generators into the backbone or pendant groups of polymers have been reported.<sup>22-26)</sup>

The purpose of this thesis is to elucidate the extreme ultraviolet sensitization

mechanism of polymers having onium salt as a side chain. This thesis is composed of the following three chapters.

In chapter 1, the radiation-induced reactions of anion-bound polymer in cyclohexanone were studied by nanosecond pulse radiolysis to clarify the elemental reactions associated with the ABP. The electron and hole transfer were discussed on the basis of the experimental results.

In chapter 2, the radiation-induced reactions in ABP films were investigated, using EUV and  $\gamma$  radiolysis to clarify the acid generation mechanism. The experimental results were discussed on the basis of kinetics obtained using the electron pulse radiolysis of model solutions.

In chapter 3, I modeled the proposed acid generation mechanisms of anion-bound resists and developed a simulation code for facilitating the development and improvement of resist materials and processes for EUV lithography. The experimental quantum efficiency of acid generation was analyzed using the developed simulation code. The validity of the obtained parameters (the thermalization distance of secondary electrons, the effective reaction radius for the reaction between phenyl radicals, and the acid generation efficiency from the excited states) was discussed.

Finally, the results obtained in each chapter were summarized.



## References

1. J. Barden, and W. H. Brattain, Phys. Rev. **74**, (1948) 230.
2. W. Shockley, and A. R. Philips, Phys. Rev. **74**, (1948) 232.
3. International Technology Roadmap for semiconductors 2013 update.  
<http://www.itrs.net/Links/2013ITRS/2013Chapters/2013Litho.pdf>
4. Y. Ekinici, M. Vockenhuber, M. Hojeij, L. Wang, and N. Mojarad, Proc. SPIE **8679**, (2013) 867910.
5. H Ito, and C. G Willson, Polym. Eng. Sci. **23**, (1983) 1012.
6. J. L. Dektar, and N. P. Hacker, J. Am. Chem. Soc. **112**, (1990) 6004.
7. Y. Matsui, H. Sugawara, S. Seki, T. Kozawa, S. Tagawa, and T. Itani, Appl. Phys. Express. **1**, (2008) 036001.
8. T. Kozawa, Y. Yoshida, M. Uesaka, and S. Tagawa, Jpn. J. Appl. Phys. **31**, (1992) 4301.
9. T. Kozawa and S. Tagawa, Jpn. J. Appl. Phys. **49**, (2010) 030001.
10. T. Kawakami, T. Nagai, Y. Nishimura, M. Shima, S. Kusumoto, and T. Shimokawa, Proc. SPIE **6519**, (2007) 65193K.
11. G. M. Schmid, M. D. Stewart, C. Wang, B. D. Vogt, V. M. Prabhu, E. K. Lin, and C. G. Willson, Proc. SPIE **5376**, (2004) 333.

12. Y. Tanaka, Y. Kikuchi, D. Goo, and I. Nishiyama, Proc. SPIE **6517**, (2007)  
65172L.
13. Y. Utsumi, T. Seshimo, Y. Komuro, A. Kawaue, K. Ishiduka, K.  
Matsuzawa, H. Hada, and J. Onodera, Jpn. J. Appl. Phys. **48**, (2009)  
06FC07.
14. H. Tsubaki, T. Tsuchihashi, and T. Tsuchimura, Proc. SPIE **7273**, (2009)  
72731K.
15. D. van Steenwinckel, J. H. Lammers, L. H. Leunissen, and J. A. J.  
Kwinten, Proc. SPIE **5753**, (2005) 269.
16. B. D. Vogt, S. Kang, V. M. Prabhu, A. Rao, E. K. Lin, S. K. Satija, and K.  
Turnquest, Proc. SPIE **6153**, (2006) 615316.
17. G. M. Wallraff, C. E. Larson, N. Fender, B. Davis, D. Medeiros, J. Meute,  
W. M. Lamanna, M. J. Parent, T. Roveledo, and G. Young, Proc. SPIE  
**4690**, (2002) 160.
18. S. Yoshizawa and J. Moriya, J. Vac. Sci. Technol. B **20**, (2002) 1342.
19. J. L. Lenhart, D. A. Fischer, S. Sambasivan, E. K. Lin, R. L. Jones, C. L.  
Soles, W. Wu, D. L. Goldfarb, and M. Angelopoulos, Langmuir **21**, (2005)  
4007.

20. T. Hirayama, D. Shiono, S. Matsumaru, T. Ogata, H. Hada, J. Onodera, T. Arai, T. Sakamizu, A. Yamaguchi, H. Shiraishi, H. Fukuda, and M. Ueda, *Jpn. J. Appl. Phys.* **44**, (2005) 5484.
21. T. Fukuyama, T. Kozawa, S. Tagawa, R. Takasu, H. Yukawa, M. Sato, J. Onodera, I. Hirose, T. Koganesawa, and K. Horie, *Appl. Phys. Express.* **1**, (2008) 065004.
22. S. Tarutani, H. Tsubaki, H. Takahashi, T. Itou, K. Matsunaga, G. Shiraishi, and T. Itani, *Proc. SPIE* **7639**, (2010) 763910.
23. R. D. Allen, U. Schaedeli, D. R. McKean, and S. A. MacDonald, *Polym. Mater. Sci. Eng.* **61**, (1981) 185.
24. J. E. Hanson, E. Reichmanis, F. M. Houlihan, and T. X. Neenan, *Chem. Mater.* **4**, (1992) 837.
25. G. M. Wallraff and W. D. Hinsberg, *Chem. Rev.* **99**, (1999) 1801.
26. M. D. Stewart, H. V. Tran, G. M. Schmid, T. B. Stachowiak, D. J. Becker, and C. G. Willson, *J. Vac. Sci. Technol. B* **20**, (2002) 2946.

## **Chapter 1**

# **Electron and Hole Transfer in Anion-Bound Chemically Amplified Resists Used in Extreme Ultraviolet Lithography**

## 1.1. Introduction

Anion-bound polymers (ABPs) in which the anion part of onium salts (acid generators) is polymerized, have attracted much attention as a key to solving the RLS trade-off problem by reducing the acid diffusion length. However, the anion-bound chemically amplified resists are generally low sensitive to radiations. A reason for the low sensitivity was considered to be due to the immobile acids. The catalytic chain reactions in anion-bound chemically amplified resists have been investigated by analyzing the line-and-space patterns fabricated with an EUV exposure tool. On the basis of experimental and simulation results, a proton diffusion model has been proposed.<sup>1)</sup> Even if the anions of acids are bound to resist polymers, the protons of acids are considered to move in the resist matrix although the moving range is restricted by the electric fields produced by the anions. In this study, I focused on not acid diffusion but acid generation in anion-bound resists as a reason for the low sensitivity. To elucidate the EUV sensitization mechanism of ABP, it is necessary to clarify the elemental reactions induced by ionizing radiations. ABP contains onium salt unit having cation and anion in the polymer. In primary processes of radiation chemistry, the dynamics of short-lived species such as radical cations and electrons play an important role. The nanosecond pulse radiolysis is a powerful method to directly probe the

radiation-induced reactions, as shown in Fig. 1-1. In the pulse radiolysis, short-lived intermediates are generated by injecting an ultrashort radiation pulse such as an electron pulse into a sample. The generated intermediates are detected by measuring photoabsorption or photoemission. In the case of photoabsorption measurement, high energy electrons ( $\sim$ MeV) are generally used to obtain a signal with sufficient intensity. The use of high penetration power of high energy radiation enables the increase of optical length, that is, the signal intensity. By changing the wavelength, the transient spectra of intermediates are also obtained.

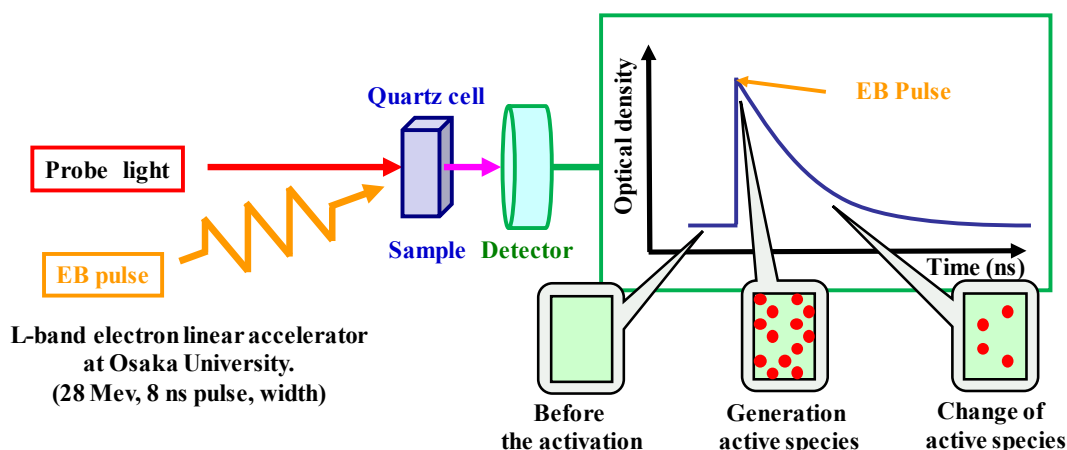


Figure 1-1. Schematic diagram of pulse radiolysis.

In this chapter, the radiation-induced reactions of anion-bound polymer were studied by nanosecond pulse radiolysis to clarify the elemental reactions associated with ABP. Although pulse radiolysis should be performed in the thin film ( $\sim$ 100 nm thick), it is difficult to detect the weak signals of intermediates generated in thin films. Using

cyclohexanone solution, the elemental reactions of ABP such as electron and hole transfer were investigated in this chapter.

## 1.2. Experiment

### 1.2.1 Material

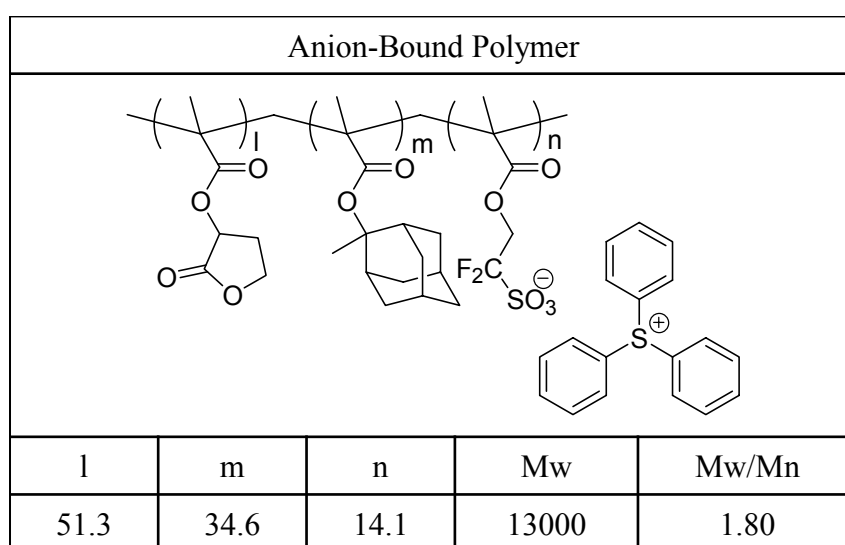


Figure 1-2. Molecular structure of anion-bound polymer.

An anion-bound polymer shown in Fig. 1-2 was used. The anion-bound polymer was composed of 14.1 mol% triphenyl sulfonium fluoroalkyl sulfonate-containing methacrylate monomers, 51.3 mol%  $\gamma$ -butyrolactone methacrylate, and 34.6 mol% 2-methyladamantyl-2-methacrylate. The weight-average molecular weight (Mw) and molecular weight distribution (Mw/Mn) were 13,000 and 1.8, respectively, determined by gel permeation chromatography against polystyrene standards. The anion-bound

polymer was dissolved in cyclohexanone (CH). The samples were deaerated in quartz cells with a 2-cm light path by Ar bubbling. The concentration of the anion-bound polymer was adjusted so that the concentration of the triphenylsulfonium fluoroalkylsulfonate unit is 30 or 50 mM. The other additives employed were purchased from Wako Pure Chemical Industries and used without further purification.

### **1.2.2. Nanosecond electron pulse radiolysis - kinetics**

Pulse radiolysis was performed by using electron pluses from LINAC at the Institute of Scientific and Industrial Research, Osaka University (28 MeV, 8 ns pulse width) as an excitation source. A Xe flash lamp (EG&G) was used as an analyzing light source. The analyzing light was transmitted to the optic lens and mirrors, sample cell, monochromator (Ritsu MC-10N), and a photodiode [Si (350–950 nm), Hamamatsu]. The signals were measured using a digital oscilloscope (Tektronix DPO7254). The kinetic and spectroscopic data were obtained by analyzing a series of traces of Xe flash lamp light. The details of nanosecond pulse radiolysis system have been reported elsewhere.<sup>2)</sup> The target chemical compounds such as ABP were dissolved in CH. The samples were deaerated in quartz cells with a 2-cm light path by Ar bubbling. The sample solutions in quartz cells were irradiated with electron pulses at room temperature.



### 1.2.3. HPLC measurement condition

The decomposition products were analyzed by high-performance liquid chromatography (HPLC). A solution of 60 vol% acetonitrile and 40 vol% water with 0.1 wt% trifluoroacetic acid was used as the eluent. The column, flow rate, introduction amount, and observed wavelength were spereiorex ODS 4.6 mm × 250 mm (Shiseido), 1.0 ml/min, 2.0 μL, and 210 nm, respectively.

## 1.3. Result and discussion

### 1.3.1 Nanosecond pulse-radiolysis of cyclohexanone

The transient absorption spectra obtained in pure CH at 0, 20, and 300 ns after the electron pulse application is shown in Fig. 1-3(a). A broad absorption was observed in pure CH in the wavelength region of near 400 nm. Upon exposure to an electron pulse, CH was ionized and electrons are emitted. The ejected electrons mostly recombine with CH radical cations (and/or their decomposition products) if they do not react with CH as follows:



To identify the intermediates with the broad absorption, triethylamine (TEA) and

TPS-TF were added to CH solutions. Figure 1-3(b) shows the effects of TEA and TPS-TF on the kinetic traces of intermediates in CH solutions monitored at the wavelength of 400 nm.

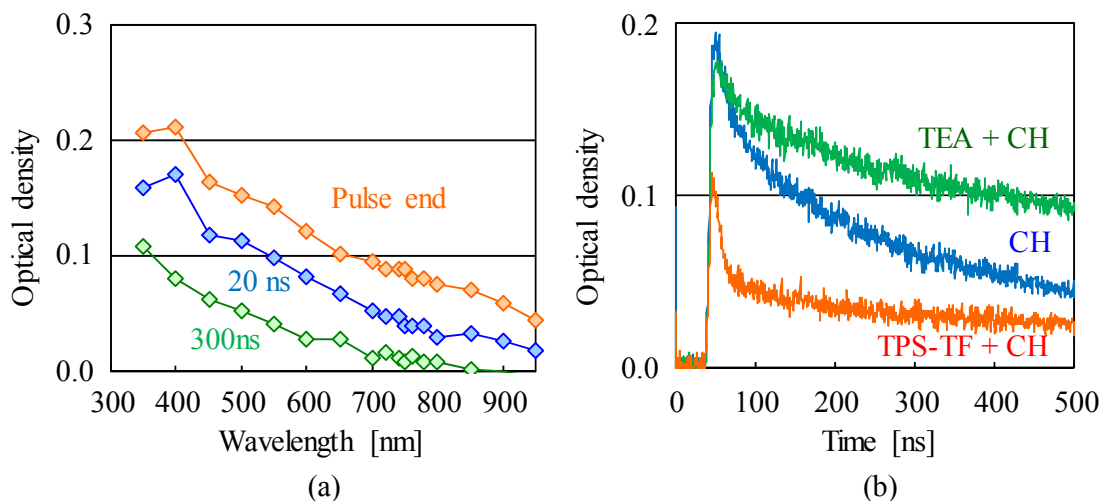


Figure 1-3. (a) Transient absorption spectra obtained in pulse radiolysis of pure CH at 0, 20, and 300 ns after an electron pulse. (b) Kinetic traces obtained in pulse radiolysis of CH solutions with no additives, 30mM TEA, and 30mM TPS-TF, monitored at the wavelength of 400 nm.

TEA and TPS-TF are a well-known cation and electron scavengers, respectively. The decay was accelerated upon the addition of TPS-TF. On the other hand, the decay was deaccelerated by adding TEA. Therefore, this intermediate is a negatively charged species, namely a solvated electron or a radical anion. The peak wavelength of broad absorption is considered to be less than 400 nm, although it was not confirmed because of the low photo transmission of pure CH at the wavelength of <400 nm. Because the peak wavelengths of solvated electrons are generally in the infrared wavelength region,

this intermediate species is likely to be a CH radical anion. The formation reaction can be assumed as follows:



The decay observed at the wavelength of 400 nm in pure CH is considered to be due to the recombination between radical cations and radical anions.



The accelerated decay upon the addition of TPS-TF is expressed as



The deaccelerated decay upon the addition of TEA is considered to be caused by the replacement of positively charged species from CH radical cations to TEA radical cations, expressed as:



The decay of CH radical anions became slower because the mobility of TEA radical cation is lower than that of CH radical cations.

### **1.3.2. Nanosecond pulse-radiolysis of anion-bound polymer**

Figure 1-4(a) shows the kinetic traces obtained in pulse radiolysis of 0, 5, 10, 20 and 30 mM ABP, monitored at the wavelength of 400 nm. By adding an anion-bound polymer, the initial yield of CH radical anions decreased and its decay became fast. These behaviors suggest the following reactions:



Here,  $\text{TPS}^+ \text{-ABP}^-$ ,  $\text{ABP}^-$ , and  $\text{TPS}^+$  represent the anion-bound polymer, its anion, and a triphenylsulfonium cation, respectively. In the reaction equations, ABP is, hereafter, expressed as  $\text{TPS}^+ \text{-ABP}^-$  to clarify the reaction schemes. The accelerated decay corresponds to reaction (1-8). The decrease in the initial yield of CH radical anions suggests a reaction with a precursor of the CH radical anion, that is, an electron. Therefore, the kinetics observed in the presence of the anion-bound polymer supports the assignment of the intermediate species to the radical anion. The transient absorption spectra obtained in the pulse radiolysis of 30 mM ABP solution in CH at 0, 20, and 300 ns after the electron pulse is shown in Fig. 1-4(b). The absorption band, the peak wavelength of which is approximately 750 nm, was observed. At the wavelength of 750 nm, a slow formation after spike-like signal was observed as shown in Fig. 1-4(c). Figure 1-4(d) shows the kinetic traces obtained by subtracting the overlapping component (the broad band spectrum of solvent) from the kinetic traces at the wavelength of 750 nm. To identify the intermediate species observed at the wavelength of 750 nm, TEA was added to the sample solution as shown in Fig. 1-5(a). By adding TEA, the slow formation of the intermediate species was inhibited and decay rate

increased with TEA concentration.

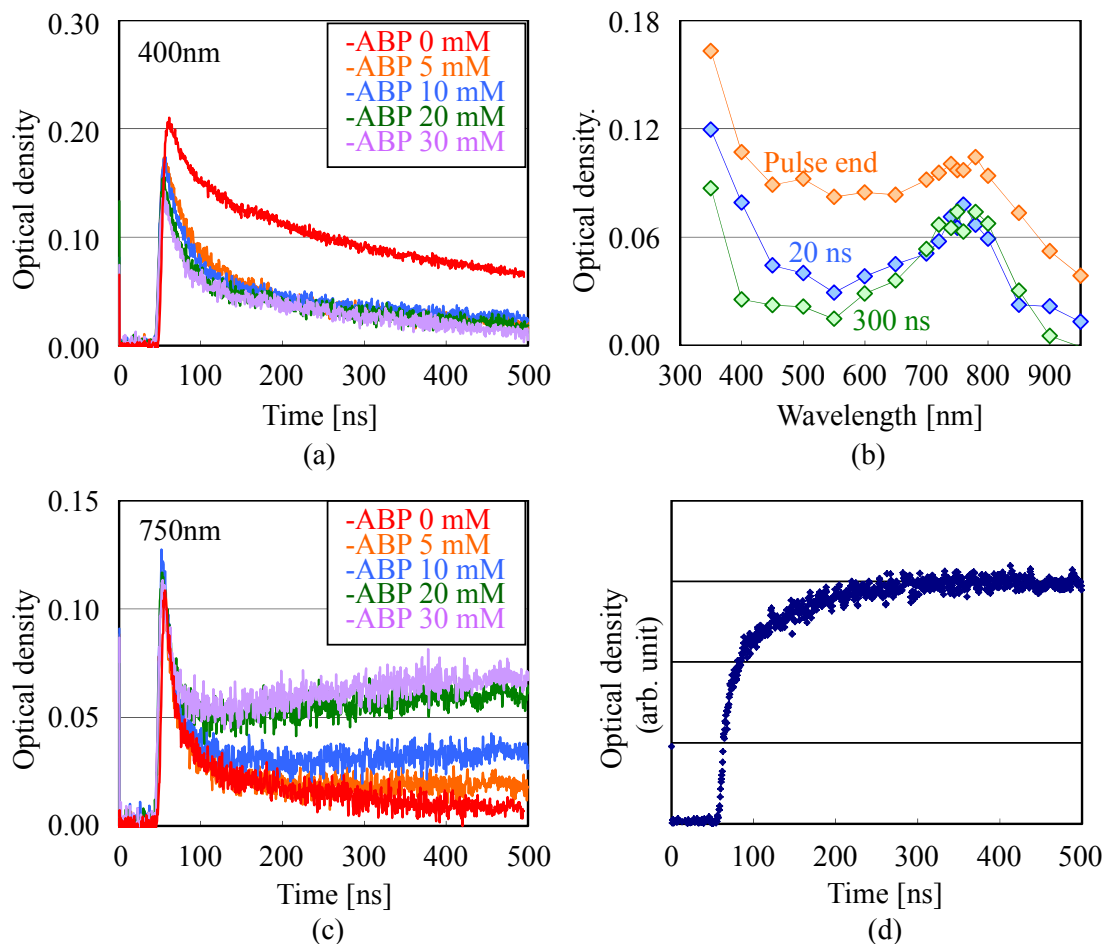


Figure 1-4. (a) shows the kinetic traces obtained in pulse radiolysis of 0, 5, 10, 20 and 30 mM ABP, monitored at the wavelength of 400 nm. (b) Transient absorption spectra obtained in pulse radiolysis of 30 mM ABP solution in CH at 0, 20, and 300 ns after an electron pulse. (c) shows the kinetic traces obtained in pulse radiolysis of 0, 5, 10, 20 and 30 mM ABP, monitored at the wavelength of 750 nm. (d) shows differential kinetic traces obtained by subtracting the overlapping component (the broad band spectrum of solvent) from the kinetic traces of 30 mM anion-bound polymer solutions in CH at the wavelength of 750 nm.

Therefore, the intermediate species is a cationic species. The rate constant for the hole transfer was roughly estimated to be  $3 \times 10^8 \text{ M}^{-1} \text{ s}^{-1}$  from the dependence of the observed

rate constants on TEA concentration. The irradiated sample was analyzed by HPLC as shown in Fig. 1-5(b). It was confirmed that diphenylsulfide was included in the decomposition products. Also, this intermediate species shows a similar spectrum to the radical cation of diphenylsulfide.<sup>3)</sup>

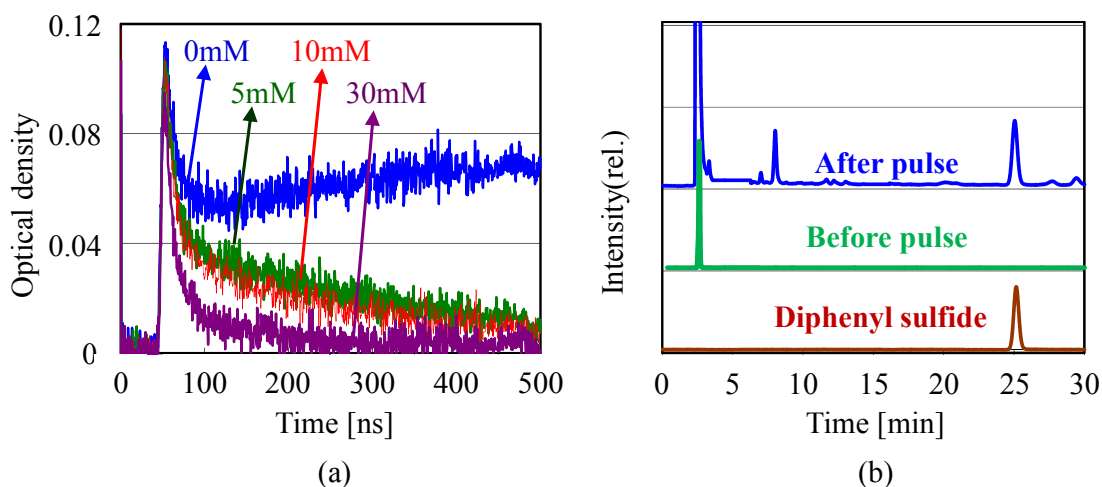


Figure 1-5. (a) Kinetic traces obtained in pulse radiolysis of 30 mM anion-bound polymer solution in CH with and without TEA and (b) HPLC chromatogram of irradiated 30 mM anion-bound polymer solution in CH. The measured wavelength of pulse radiolysis was 750 nm. The numerical values in mM in (a) represent the TEA concentration.

Therefore, reaction (1-7) and (1-8) can be written more explicitly as follows:



Here,  $\text{Ph}_2\text{S}$  and  $\text{Ph}^\cdot$  represent the DPS, a phenyl radical, respectively. Thus, the slow formation after spike-like signal is due to DPS radical cations. The yield of DPS radical cations increased with ABP concentration as shown in Fig. 1-4(c). The spike-like

signals in Fig. 1-4(c) are possibly due to electrons. Because the observed decay was close to the time resolution of pulse radiolysis, the rate constant (1-9) was undetermined. The reaction of ABP with electrons has been evaluated in acetonitrile solution.<sup>4)</sup> The rate constant for the reaction of ABP with electrons in acetonitrile was  $4.0 \times 10^{10} \text{ M}^{-1} \text{ s}^{-1}$ . The rate constants for the reaction of TPS-TF and TPS-ItBu, both of which are low molecular weight acid generators, with electrons were  $6.0 \times 10^{10} \text{ M}^{-1} \text{ s}^{-1}$ . The rate constant of ABP was two third of that of low molecular weight acid generators. Because the low mobility of ABP partly account for the low rate constant, the reactivity of ABP with electrons does not significantly differ from that of TPS-TF.

Nagahara et al. reported that a diphenylsulfide radical cation is generated when triphenylsulfonium salt solution in acetonitrile is irradiated by an electron beam under high concentration condition (100-500 mM). It has been suggested that the diphenylsulfide radical cation is generated though direct electronic excitation upon exposure to an electron pulse.<sup>5)</sup> However, the contribution of direct electronic excitation is minor because the concentration was set low in this study. The DPS radical cation is unlikely to be generated through the direct electronic excitation of anion-bound polymers, because the lifetime of excited triphenylsulfonium salt is less than 1 ps.<sup>6)</sup> Therefore, DPS radical cations were generated through the hole transfer from CH radical

cations to DPS as follows:



Although no radical cation of the anion-bound polymer was observed in this study, the anion-bound polymer is directly ionized to form a radical cation when the anion-bound polymer is irradiated by ionizing radiation under film condition. Because the proton is a positively charged species, its origin in acid generation is generally a radical cation generated directly or indirectly by the ionizing radiation. Therefore, the dynamics of holes generated through ionization is essential to acid generation. Because the radical cation of diphenylsulfide is stable, it is unlikely to be spontaneously deprotonated. For proton generation from the radical cation of diphenylsulfide, an additional reaction with a reactive intermediate such as recombination with a phenyl radical is required. This reaction path possibly occurs in a polystyrene film with triphenylsulfonium triflate. However, it has been reported that the acid generation efficiency in such a system is low.<sup>7,8)</sup> Therefore, the slow formation of the radical cation of diphenylsulfide suggests the inefficiency of the proton generation of the anion-bound polymer used in this study.

The formation of the radical cation of diphenylsulfide was further investigated by adding phenol. Phenol derivatives are a well-known proton source for resist materials.<sup>9,10)</sup> Radical cations of phenol derivatives undergo an ion molecular reaction



with neutral phenol derivatives to produce proton adducts. The proton is generated through the hole transfer from DPS radical cations to phenol as follows:

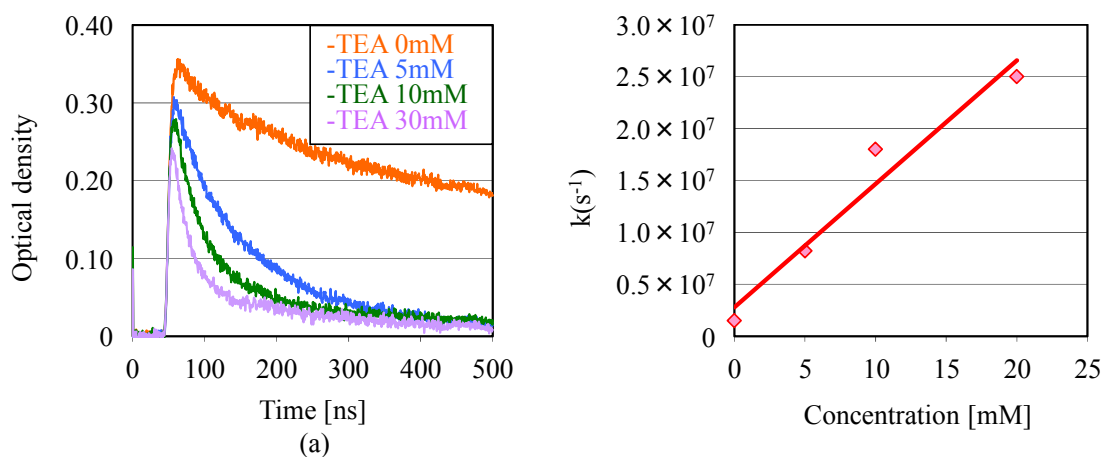
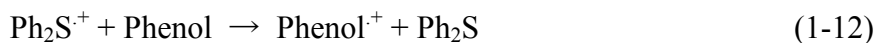


Figure 1-6. (a) Kinetic traces obtained in pulse radiolysis of 30 mM DPS solutions in CH with 0, 5, 10, and 30 mM TEA. (b) Dependence of observed decay rate  $k$  on the concentration of TEA.

On the other hand, a basic compound, called a quencher, is generally added to control the acid diffusion during postexposure baking (PEB) in chemically amplified resists. Therefore, the phenolic hydroxy group and amine compound generally coexist in chemically amplified resists. The rate constants for the reactions of DPS radical cations with TEA and phenol were estimated. Here, DPS radical cations were intentionally generated by adding DPS in CH solutions, to precisely evaluate the rate constants. Figure 1-6(a) shows the kinetic traces of DPS radical cations with and without TEA. In

the absence of TEA, DPS radical cations were generated through the reaction of the hole transfer from CH radical cations to DPS [reaction (1-11)] upon exposure to an electron pulse. By increasing the TEA concentration, the decay rate increased. The observed decay rate was plotted in Fig. 1-6(b). From the slope of the graph in Fig. 1-5(b), the rate constant for the reaction of DPS radical cations with TEA was calculated to be  $1.2 \times 10^9 \text{ M}^{-1}\text{s}^{-1}$ . Similarly, the reaction of DPS radical cations with phenol was measured as shown in Fig. 1-7.

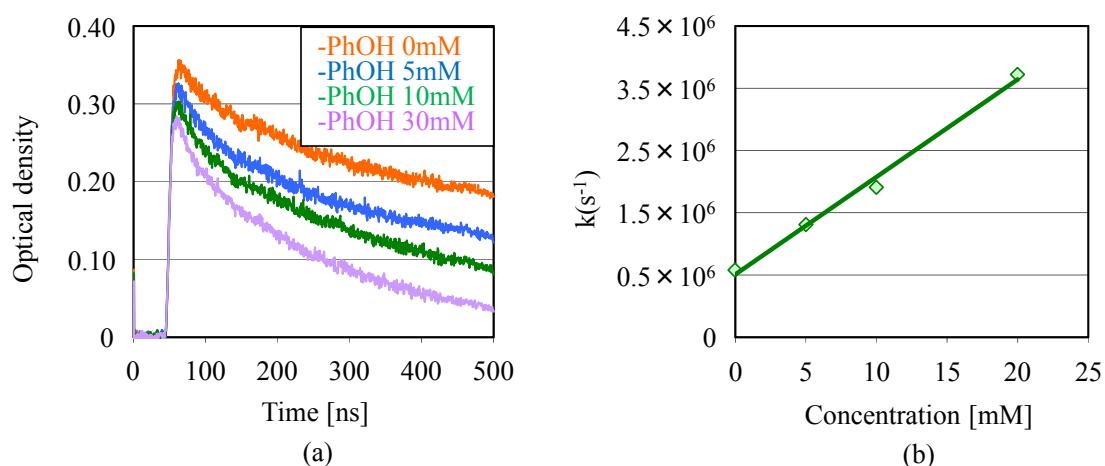


Figure 1-7. (a) Kinetic traces obtained in pulse radiolysis of 30 mM DPS solutions in CH with 0, 5, 10, and 30 mM phenol. (b) Dependence of observed decay rate  $k$  on the concentration of phenol.

From the slope of the graph in Fig. 1-7(b), the rate constant for the reaction of DPS radical cations with phenol was calculated to be  $1.6 \times 10^8 \text{ M}^{-1}\text{s}^{-1}$ . This result indicates that the formation of DPS radical cation is suppressed in the presence of a typical proton source for the acid generation in chemically amplified resists, phenol. This result

suggested that the efficiency of hole transfer to a proton source (phenol) was lower than that to a quencher (TEA). From the viewpoint of acid generation, the efficiency of hole transfer to the proton source should be increased. The requirement for the proton source is that the pKa of its radical cation is sufficiently low.<sup>11)</sup> Note that electrons generated through ionization should also be transferred to the anion source (acid generator) as much as possible.<sup>12)</sup>

#### **1.4. Summary**

The electron and hole transfer induced in the anion-bound polymer solution in CH was investigated. For efficient acid generation by ionizing radiation, the electron and hole generated through ionization should be efficiently transferred to the anion and proton sources, respectively. Although the electron was transferred to the anion-bound polymer, the hole was captured by diphenylsulfide, which is a decomposition product of the anion-bound polymer and a non-proton source. It was confirmed that the formation of the radical cation of diphenylsulfide is suppressed in the presence of a well-known proton source for resist materials (phenol). Currently, the enhancement of resist performance is required for its application to the sub-10 nm node. The design of an efficient electron and hole transfer system is essential for the enhancement of resist

performance. In particular, the development of a proton source that can trap holes generated in the matrix more efficiently than phenol derivatives is an urgent task.

## References

- 1) T. Kozawa, J. J. Santillan, and T. Itani, *Appl. Phys. Express.* **5**, (2012) 074301.
- 2) S. Seki, Y. Yoshida, S. Tagawa, and K. Asai, *Macromolecules.* **32**, (1999) 1080.
- 3) T. Shida, *Electronic Absorption Spectra of Radical Ions* (Elsevier, New York, 1988).
- 4) S. Enomoto, D. T. Nguyen, and S. Tagawa, *Jpn. J. Appl. Phys.* **52**, (2013) 06GC03.
- 5) S. Nagahara, T. Kozawa, Y. Yamamoto, and S. Tagawa, *J. Photopolym. Sci. Technol.* **11**, (1998) 577.
- 6) S. Tagawa, S. Nagahara, T. Iwamoto, M. Wakita, T. Kozawa, Y. Yamamoto, D. Werst, and A. D. Trifunac, *Proc. SPIE* **3999**, (2000) 204.
- 7) H. Yamamoto, A. Nakano, K. Okamoto, T. Kozawa, and S. Tagawa, *Jpn. J. Appl. Phys.* **43**, (2004) 3971.
- 8) H. Yamamoto, T. Kozawa, S. Tagawa, H. B. Cao, H. Deng, and M. J. Leeson, *Jpn. J. Appl. Phys.* **46**, (2007) L142.
- 9) T. Kozawa, S. Nagahara, Y. Yoshida, S. Tagawa, T. Watanabe, and Y. Yamashita, *J. Vac. Sci. Technol. B* **15**, (1997) 2582.
- 10) A. Nakano, T. Kozawa, K. Okamoto, S. Tagawa, T. Kai, and T. Shimokawa, *Jpn. J. Appl. Phys.* **45**, (2006) 6866.

11) T. Kozawa and S. Tagawa, Jpn. J. Appl. Phys. **49**, (2010) 030001.

12) T. Kozawa and S. Tagawa, Jpn. J. Appl. Phys. **47**, (2008) 8328.

## **Chapter 2**

### **Acid generation mechanism in anion-bound chemically amplified resists used for extreme ultraviolet lithography**

## **2.1. Introduction**

In Chapter 1, the elemental reactions associated with ABP were clarified on the basis of electron pulse radiolysis of model solution. However, the radiation-induced reactions in solid films generally differ from those in solutions. This is mainly caused by the difference in the reaction conditions such as molecular diffusion between solution and film (solid). To elucidate the reaction mechanisms in the solid films, it is necessary to perform the experiments using the thin film.

In this chapter, I have investigated the radiation-induced reactions in ABP films using EUV and  $\gamma$  radiolysis to clarify the acid generation mechanism. The experimental results were discussed on the basis of kinetics obtained using the electron pulse radiolysis of model solutions in chapter 1.

## **2.2. Experimental**

### **2.2.1. Material**

An anion-bound polymer shown in Figure 2-1 was used. The composition ratio of triphenylsulfonium fluoroalkylsulfonate units was changed from 5.4 to 10.9 and 14.1 mol%. The composition ratio was determined by NMR spectra. The weight-average molecular weight ( $M_w$ ) and molecular weight distribution ( $M_w/M_n$ ) were determined



by gel permeation chromatography against polystyrene standards. In this study, the polymers shown in Fig. 2-1 are hereafter called 5, 10, and 14 mol% ABP, respectively. Poly(4-hydroxy styrene) (PHS) were purchased from Toho Chemical Industry. Coumarin6 (C6) were purchased from Tokyo Chemical Industry Co., Ltd. The other additives employed were purchased from Wako Pure Chemical Industries and used without further purification.

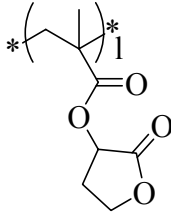
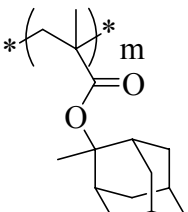
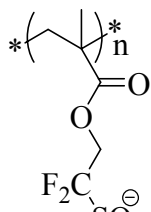
Anion-Bound Polymer					
					
	l	m	n	Mw	Mw/Mn
ABP 5 mol%	47.5	47.1	5.4	12500	2.12
ABP 10 mol%	46.3	42.8	10.9	12700	1.84
ABP 14 mol%	47.0	38.7	14.3	13000	1.80

Figure 2-1. Molecular structure of anion-bound polymer.

### 2.2.2. EUV radiolysis - acid yield

The acid yield upon exposure to EUV radiation was measured using an acid-sensitive dye, C6, the proton adducts of which have a characteristic optical absorption band around the wavelength of 533 nm.<sup>1,2)</sup> ABP and C6 were dissolved in a mixture of

tetrahydrofuran, CH, and  $\gamma$ -butyrolactone. The solvent ratio was 16 : 74 : 10. The weight ratio of the constituents was ABP:C6=100.0:5.0. The solutions were spin-coated onto quartz substrates at 1500 rpm for 30 s to form thin films. Subsequently, the films were baked at 90.0 °C for 90 s before the exposure to EUV (Energetic EQ-10M). The film thickness was adjusted to be more than 1.3  $\mu\text{m}$  so that more than 98% of incident EUV photons were absorbed by the film. After the exposure to EUV, the absorption spectra were recorded using a JASCO V-570 spectrophotometer to quantify acid yields in the polymer films. Similarly, the acid yields generated in PHS films containing triphenylsulfonium- triflate (TPS-TF) were evaluated for comparison. The weight ratios of the constituents were PHS : TPS-TF : C6=100.0 : 19.5 : 5.0 and 100.0 : 58.2 : 5.0. The exposure dose was calibrated by comparing the measured quantum efficiency in the PHS film containing 10 wt% TPS-TF with the reported value (2.63).<sup>2)</sup>

### **2.2.3. $\gamma$ radiolysis - product analysis**

ABP was dissolved in a mixture of 1-methoxy-2-propyl acetate (PGMEA), 1-methoxy-2-propanol (PGME), and CH. The solvent ratio was 2 : 3 : 5. The solutions were spin-coated onto Si substrates at 1500 rpm for 30 s to form thin films. Subsequently, the films were baked at 90.0 °C for 60 s before exposure. The film thickness was adjusted to be approximately 300 nm. The samples were exposed to  $\gamma$ -

rays from  $^{60}\text{Co}$  source because EUV source power is too weak to induce sufficient amount of chemical reactions for product analysis. The absorbed dose was 389 kGy. This absorbed dose corresponds to the exposure dose of approximately  $100 \mu\text{C}/\text{cm}^2$  for 75 keV electron beam, which was estimated with the reported data.<sup>3)</sup> The irradiated materials scraped from Si substrates were analyzed with high-performance liquid chromatography (HPLC).

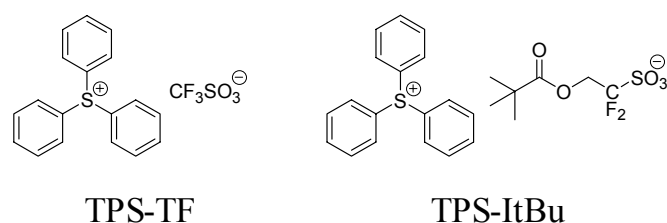


Figure 2-2. Molecular structures of TPS-TF and TPS-ItBu.

A solution of 60 vol% acetonitrile and 40 vol% water with 0.1 wt% trifluoroacetic acid was used as an eluent. The column, flow rate, introduction amount, and observed wavelength were spereiorex ODS 4.6 mm  $\times$  250 mm (Shiseido), 1.0 ml/min, 2.0  $\mu\text{L}$ , and 210 nm, respectively. PHS and tri-n-octylamine (TOA) were used as additives. Similarly, decomposition products in PHS films were analyzed for comparison. Triphenylsulfonium-1,1-difluoro-2-(pivaloyloxy) ethansulfonic acid salt (TPS-ItBu) and TPS-TF were used as additives. The chemical structures of TPS-ItBu and TPS-TF are shown in Figure. 2-2. TPS-TF solution in acetonitrile was also exposed to  $\gamma$ -rays for the HPLC analysis of decomposition products. This experiment was carried out for the

comparison with the previous study.<sup>4)</sup>

### 2.3. Results and discussion

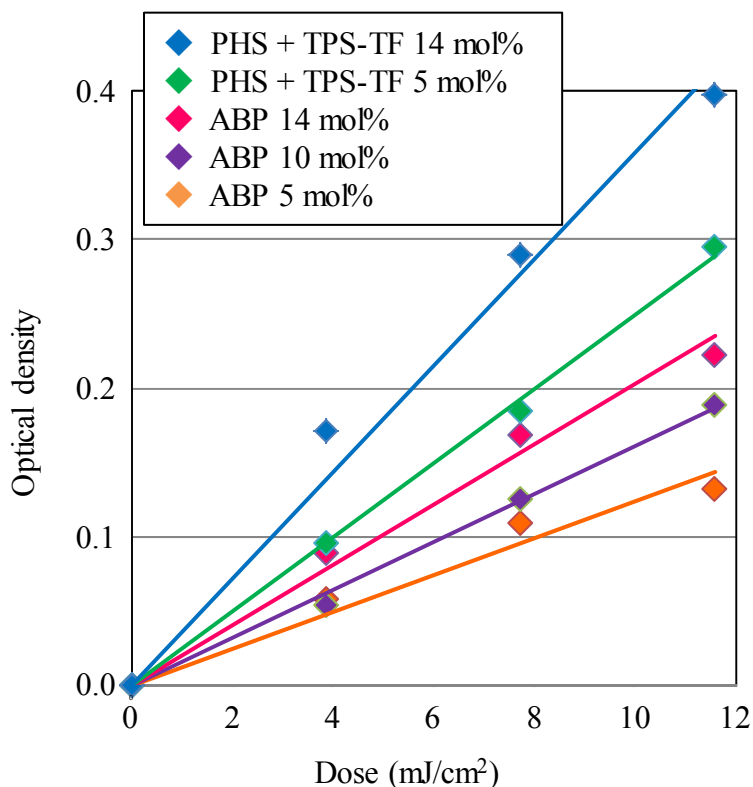


Figure 2-3. Dependence of optical density observed in the sample films with C6 after the exposure to EUV radiation. The samples used were 5, 10, and 14 mol% ABP films and PHS films with 5 and 14 mol% TPS-TF.

The acid yields generated upon exposure to EUV were measured using C6. Figure 2-3 shows the exposure dose dependence of the absorption intensity of C6 proton adducts. From the slopes of the graph, the quantum efficiencies of acid generation were calculated to be 1.7, 1.9, and 2.6 for 5, 10, and 14 mol% ABP films, respectively, in accordance with the reported procedure.<sup>3)</sup> The quantum efficiencies of acid generation

in PHS films were 3.1 and 4.8 for 5 and 14 mol% TPS-TF. The quantum efficiency in ABP films was significantly lower than that in PHS films with acid generators. The acid generation mechanisms in PHS films have been investigated in details.<sup>5,6)</sup> In PHS, the protons of acids are generated through the deprotonation of PHS radical cations, which are generated through ionization. Also, electrons are ejected from molecules upon ionization. The ejected electrons either recombine with PHS radical cations (or its decomposition products) or react with the acid generators in PHS.<sup>7)</sup> The role of acid generators is to replace thermalized electrons with stable anions and suppress the recombination of thermalized electrons with PHS radical cations.<sup>8)</sup> Almost all PHS radical cations that escape the recombination are deprotonated, assisted by the hydrogen bonding.<sup>3)</sup> It has been confirmed that the experimental proton yields in PHS films well agree with the anion yields estimated on the basis of electron dynamics in condensed matters.<sup>3,9)</sup> The reason why the quantum efficiency in ABP was lower than that in PHS seems to be the lack of effective proton sources such as phenol units. However, a significant amount of acids were still generated in ABP films. In the following sections, the acid generation mechanisms in ABP films were discussed.

On the basis of the kinetics obtained using the electron pulse radiolysis of model solutions, the decomposition mechanisms in ABP films are discussed. The sample films

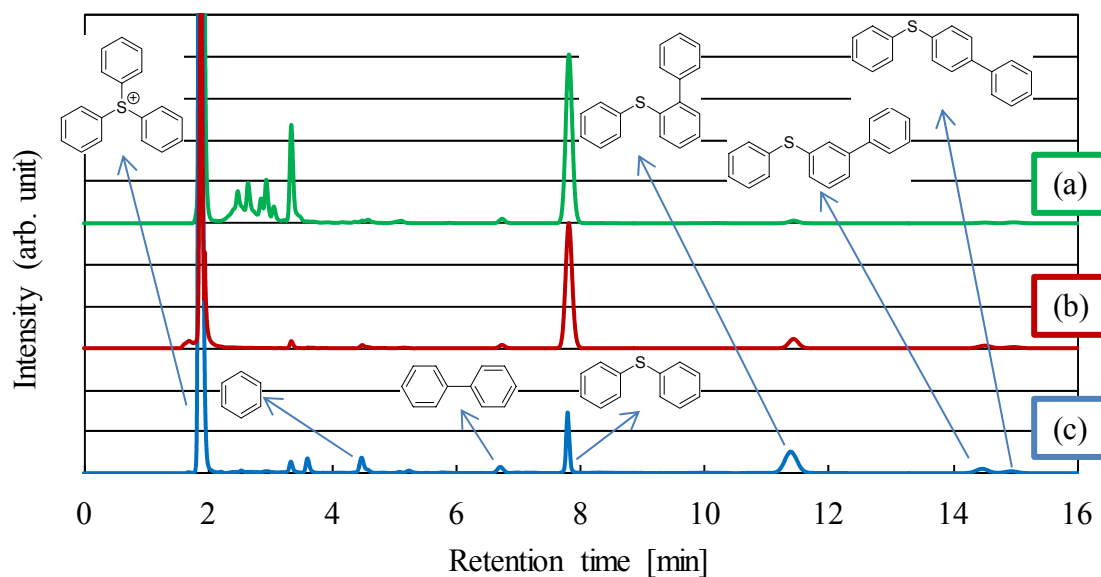
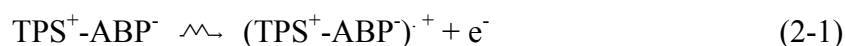


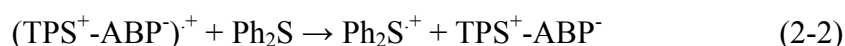
Figure 2-4. HPLC chromatogram of solution and films irradiated by  $\gamma$ -rays from  $^{60}\text{Co}$ . The irradiated samples are (a) 100 mM TPS-TF solution in acetonitrile, (b) PHS film with 14 mol% TPS-TF, and (c) 14 mol% ABP film.

spin-coated on Si wafers were exposed to  $\gamma$ -rays from  $^{60}\text{Co}$ . The exposed samples were analyzed using HPLC. Figure 2-4 shows HPLC chromatograms of 100 mM TPS-TF solution in acetonitrile, PHS film with 14 mol% TPS-TF, and 14 mol% ABP film. The analysis of 100 mM TPS-TF solution in acetonitrile was carried out for the comparison with the reported data.<sup>4)</sup> The experimental result well agreed with the reported data. As reported previously, the main decomposition product was DPS. The yields of phenyl-substituted DPS [2-(phenylthio)biphenyl, 3-(phenylthio)biphenyl, and 4-(phenylthio)biphenyl] were little. It has been reported that the phenyl-substituted dipenylsulfides are generated through the recombination between phenyl radical and DPS radical cation or between phenyl cation and DPS. The phenyl radical, DPS radical

cation, phenyl cation, and DPS are decomposition products from TPS-TF in an electronic excited state.<sup>10)</sup> In PHS films, the relative yield of 2-(phenylthio)biphenyl to DPS increased, compared with that in acetonitrile. This is because the cage escape reaction decreased in solid films due to the immobility of surrounding molecules. In ABP films, the relative yield of 2-(phenylthio)biphenyl to DPS further increased. The yield from the direct electronic excitation of acid generators (units) is not considered to significantly differ between PHS and ABP matrices. Therefore, the increase in the ratio of 2-(phenylthio)biphenyl to DPS suggests another reaction path. In ABP films, ABP molecules are mainly ionized upon exposure to ionizing radiations because they are main constituents.



As discussed for the electron pulse radiolysis of model solutions, the ejected electrons are captured by ABP after the energy of ejected electrons are sufficiently lost. DPS is generated through the dissociative electron attachment [reaction (2-1)]. In the film, the hole transfer from ABP radical cations to DPS is considered to occur on the basis of the discussion in chapter 1.



Phenyl-substituted DPS and protons can be generated through the reaction of DPS

radical cations and phenyl radicals.



The alternative reaction path is the recombination of ABP radical cations and electrons.

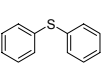
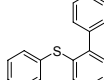
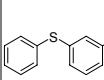
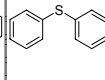
The electronic excited state of ABP can be generated through the recombination.



Here,  $(\text{TPS}^+-\text{ABP}^{\cdot-})^*$  is an electronically excited ABP. The decomposition of ABP in electronic excited state is also considered to give phenyl-substituted DPS and a proton, similarly to the case of the decomposition of TPS-TF upon exposure to DUV and VUV. However, this assumption cannot explain the difference between the ratios of phenyl-substituted DPS to DPS in PHS and ABP matrices. Also, the reaction (2-4) is considered to be suppressed in the presence of electron scavengers such as TPS-TF and ABP. The results of  $\gamma$  radiolysis including those shown in Fig. 2-4 are summarized in Table 2-1. The HPLC area data of decomposition products were normalized with the area corresponding to TPS cation. As mentioned above, the ratio of 2-(phenylthio)biphenyl yield to DPS yield increased on the order of entry 1 (TPS-TF solution in acetonitrile), entry 12 (PHS film with 14 mol% TPS-TF), and entry 4 (14 mol% ABP film).

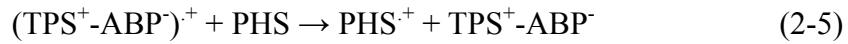


Table 2-1. HPLC area data of decomposition products normalized with area corresponding to triphenylsulfonium cation. AG and AN denotes acid generator and acetonitrile, respectively. "1 eq" denotes the molar equivalent to acid generator units.

Entry	PAG	Matrix	Additive				
1	TPS-TF	AN 100mM	None	18.78	0.39	0.14	0.21
2	5 mol% ABP		None	8.74	5.01	1.13	0.29
3	10 mol% ABP		None	8.53	5.52	1.10	0.44
4	14 mol% ABP		None	7.01	7.02	1.56	0.57
5	14 mol% ABP		PHS 0.5eq	9.57	6.38	1.39	0.52
6	14 mol% ABP		PHS 1eq	11.25	5.34	1.16	0.40
7	14 mol% ABP		PHS 2eq	13.74	5.08	1.00	0.33
8	14 mol% ABP		TOA 0.5eq	8.21	6.51	1.47	0.36
11	TPS-ItBu 14 mol%	PHS	None	14.65	2.05	0.34	0.15
12	TPS-TF 14 mol%	PHS	None	14.07	2.30	0.51	0.25

The ratio of decomposition products in PHS film with 14 mol% TPS-ItBu was similar to that in PHS film with 14 mol% TPS-TF (comparison between entries 11 and 12). TPS-ItBu is a unit structure used as an acid generator incorporated in ABP. The slight difference between the molecular structures of TPS-TF and TPS-ItBu did not affect not only the reactivity to electrons but also the decomposition products. In the comparison among entries 2-4, the ratio of 2-(phenylthio)biphenyl yield in 5, 10, and 14 mol% ABP without the normalization by TPS cation was 1.0 : 2.7 : 4.3. This trend agreed with that observed in the quantum efficiency of 5, 10, and 14 mol% ABP, although the values are not accurate without the normalization. The ratios of phenyl-substituted DPS yields to DPS yield with the normalization by TPS cation slightly increased as shown in Table 2-1. The slight increase in the ratio of phenyl-substituted DPS yields to DPS yield is considered to be caused by the increase in the concentrations of DPS radical cations and

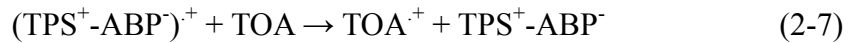
phenyl radicals. Upon the addition of PHS to 14 mol% ABP films, DPS yield increased and phenyl-substituted DPS yield decreased (entries 4-7). This is because PHS competed with DPS for the hole transfer [reaction (2-3) and (2-5)].



Also, phenol is a well-known radical scavenger. PHS is considered to compete with DPS radical cation for phenyl radicals.



Upon the addition of TOA, a similar trend to the case for PHS was observed. This is because TOA competed with DPS for the hole transfer [reaction (2-3) and (2-7)].



As discussed above, the proposed mechanism well explains the results of  $\gamma$  radiolysis. Also, the proposed acid generation mechanism well explains the reason why acids are generated in the absence of a typical proton source, phenol, although the acid generation efficiency was decreased.

The acid generation mechanism of anion-bound chemically amplified resists is summarized in Fig. 2-5. In ABP films, ABP radical cations and electrons are generated through ionization upon exposure to ionizing radiations such as EUV. ABP reacts with electrons to produce DPS and phenyl radicals through the dissociative electron

attachment. DPS radical cations are generated through the hole transfer from ABP radical cation to DPS. Phenyl-substituted DPS and protons are generated through the reaction of DPS radical cations and phenyl radicals. The efficiency of acid generation through this reaction path is lower than that in PHS films with TPS-TF because the hole transfer and the reaction of radical cations with phenyl radicals are required for the proton generation.

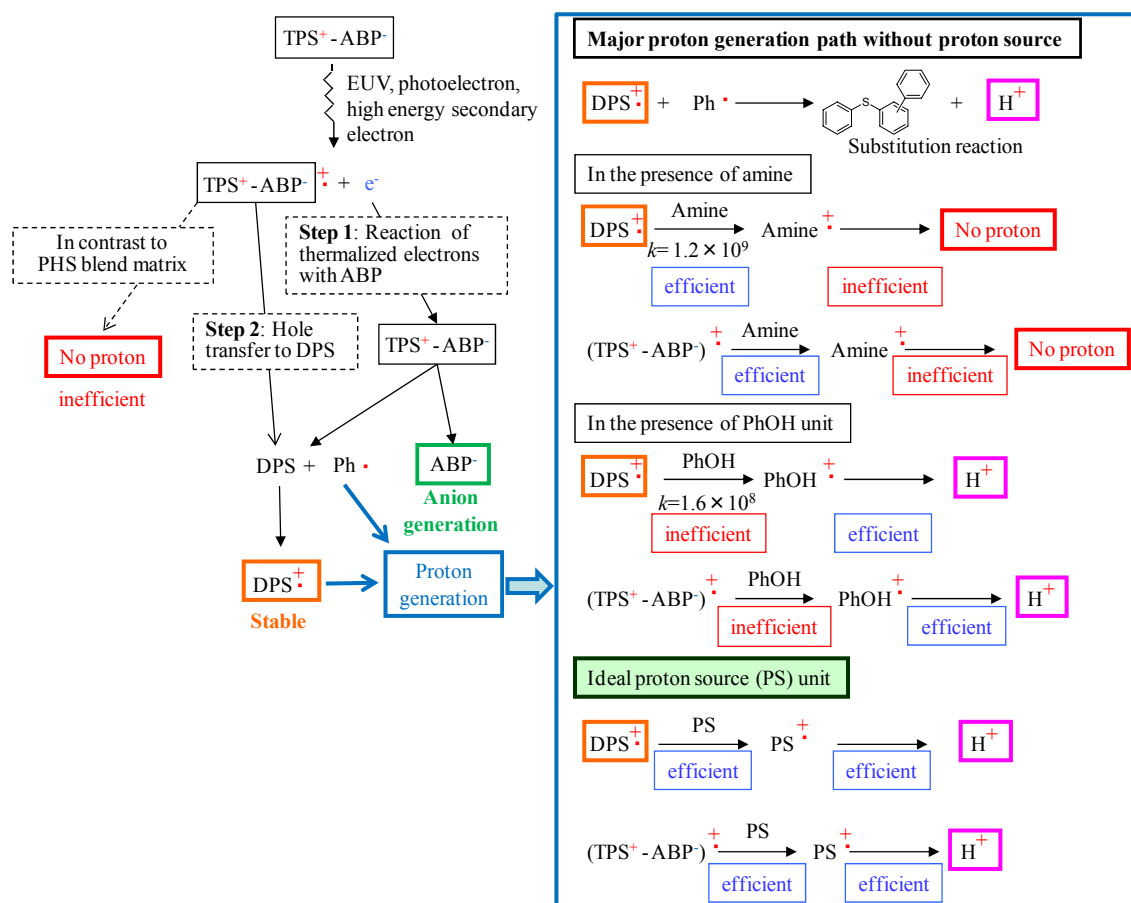


Figure 2-5. Schematic drawing of acid generation mechanism in anion-bound chemically amplified resists (in the absence of proton source). Steps 1 and 2 represent the important reactions for the generation of DPS radical cations.

In PHS films with TPS-TF, PHS radical cations (main products of ionization) are simply and efficiently deprotonated.<sup>5)</sup> Upon the addition of amines such as TEA and TOA, the hole transfer from ABP radical cations to amines results in the formation of amine radical cations that do not release protons. Upon the addition of phenols, the hole transfer from ABP radical cations to phenols is considered to be inefficient compared with the case for amines, although the phenol radical cations are efficiently deprotonated. The development of proton sources that can trap holes generated in matrix and can be efficiently deprotonated is essential to the improvement of anion-bound chemically amplified resists. In this study, the acid generation mechanisms in anion-bound chemically amplified resists were qualitatively discussed on the basis of EUV,  $\gamma$ , and electron (pulse) radiolysis. The minor differences among chemical reactions induced by these radiations have been discussed elsewhere.<sup>11)</sup>

## **2.4. Summary**

The radiation chemistry induced in ABP films was investigated using  $\gamma$  and EUV radiolysis. On the basis of experimental results, the acid generation mechanism in anion-bound chemically amplified resists was proposed. In ABP films, ABP radical cations and electrons are generated through ionization upon exposure to ionizing

radiations such as EUV. ABP reacts with electrons to produce DPS and phenyl radicals through the dissociative electron attachment. DPS radical cations are generated through the hole transfer from ABP radical cation to DPS. The major path for the proton generation in the absence of effective proton sources is considered to be the reaction of phenyl radicals with DPS radical cations.

## Reference

- 1) C. Coenjarts, J. Cameron, N. Deschamps, D. Hambly, G. Pohlers, J. C. Scaiano, R. Sinta, S. Virdee, and A. Zampini, Proc. SPIE **3678**, (1999) 1062.
- 2) G. Pohlers, J. C. Scaiano, and R. Sinta, Chem. Mater. **9**, (1997) 3222.
- 3) H. Yamamoto, T. Kozawa, A. Nakano, K. Okamoto, Y. Yamamoto, T. Ando, M. Sato, H. Komano, and S. Tagawa, Jpn. J. Appl. Phys. **43**, (2004) L848.
- 4) S. Tagawa, S. Nagahara, T. Iwamoto, M. Wakita, T. Kozawa, Y. Yamamoto, D. Werst, and A. D. Trifunac, Proc. SPIE **3999**, (2000) 204.
- 5) A. Nakano, T. Kozawa, K. Okamoto, S. Tagawa, T. Kai, and T. Shimokawa, Jpn. J. Appl. Phys. **45**, (2006) 6866.
- 6) K. Okamoto, M. Tanaka, T. Kozawa, and S. Tagawa, Jpn. J. Appl. Phys. **48**, (2009) 06FC06.
- 7) T. Kozawa, T. Shigaki, K. Okamoto, A. Saeki, S. Tagawa, T. Kai, and T. Shimokawa, J. Vac. Sci. Technol. B **24**, (2006) 3055.
- 8) T. Kozawa, Y. Yoshida, M. Uesaka, and S. Tagawa, Jpn. J. Appl. Phys. **31**, (1992) 4301.
- 9) T. Kozawa and S. Tagawa, Jpn. J. Appl. Phys. **50**, (2011) 030209.
- 10) J. L. Dektar and N. P. Hacker, J. Am. Chem. Soc. **112**, (1990) 6004.

11) T. Kozawa and S. Tagawa, Jpn. J. Appl. Phys. **49**, (2010) 030001.

## **Chapter 3**

**Modeling and simulation of acid generation in anion-bound chemically amplified  
resists used for extreme ultraviolet lithography**



### 3.1. Introduction

The performance of chemically amplified resists is basically determined by the efficiencies of photoabsorption, acid generation, and acid-catalytic reactions and the dissolution factors of resist components.<sup>1)</sup> In chemically amplified resists for deep and vacuum UV (DUV and VUV) lithography, the major path of the decomposition of acid generators is the direct sensitization by photons.<sup>2)</sup> However, the molecular selectivity of photoabsorption is largely lost in the energy region of EUV. In chemically amplified EUV resists, the efficient acid generation without the selective photoabsorption is required.<sup>3)</sup> From the viewpoint of efficiency, the acid generation process is critical for the performance of chemically amplified EUV resists.

In the previous chapters, the chemical reactions induced in ABP films were investigated with the electron pulse,  $\gamma$ , and EUV radiolysis. The decomposition products induced by secondary electrons were analyzed using  $\gamma$  radiolysis. The quantum efficiency of acids generated in ABP films was determined using EUV radiolysis. On the basis of experimental results, the acid generation path that is different from that in poly(4-hydroxystyrene) (PHS)-based resists was proposed.

In this chapter, I modeled the proposed acid generation mechanisms of anion-bound resists and developed a simulation code for facilitating the development and

improvement of resist materials and processes for EUV lithography. The experimental quantum efficiency of acid generation was analyzed using the developed simulation code. The validity of the obtained parameters (the thermalization distance of secondary electrons, the effective reaction radius for the reaction between phenyl radicals, and the acid generation efficiency from the excited states) is discussed.

## **3.2. Experimental**

### **3.2.1. X-ray diffractometer- film density**

The film densities were measured with a X-ray diffractometer (XRD, Rigaku SmartLab) to determine the concentration of acid generator units and the absorption coefficient of resist films. The sample films were prepared by dissolving ABP in a solvent consisting of 1-methoxy-2-propyl acetate (PGMEA), 1-methoxy-2-propanol (PGME), and cyclohexanone, mixed at a ratio of 45:30:25, and by spin coating the solution onto a 3-inch silicon wafer. After spin coating, the samples were baked on a hot plate at 90 °C for 60 s. X-ray was irradiated at the incident angles of 0 to 10°. X-ray reflective data were analyzed using a reflectivity analysis software tool (Rigaku Global Fit).

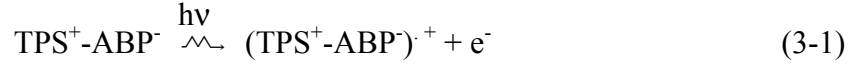
### **3.2.2. Dielectric constants**

The dielectric constants of resist films are necessary for the calculation of the dynamics of thermalized electrons. The dielectric constants of ABP films were measured by using a Solid State Measurement Mercury Probe CV system (SSM 600 CV) at 0.1 MHz. The sample films were prepared by dissolving ABP in a solvent consisting of PGMEA, and cyclohexanone, mixed at a ratio of 10:90, and by spin coating the solution onto a 6-inch low resistance silicon wafer. After spin coating, the samples were baked on a hot plate at 90 °C for 60 s and then applied to the measurement.

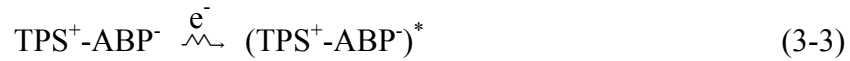
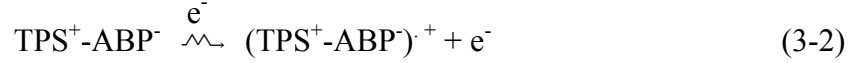
### **3.3. Simulation model**

EUV photons were assumed to be randomly injected into the target area. The exposed area was set to be  $50 \times 50 \text{ nm}^2$  in the simulation. The resist thickness was set to be 50 nm, considering the computational time. The following boundary conditions were applied for the electrons and molecules. The periodic boundary condition was applied in the horizontal direction. The reflective boundary condition was applied at the resist surface. A 20-nm-thick resist layer was added at the bottom of the target resist layer for the calculation of electron and molecule trajectories near the bottom of the target resist layer. The injected EUV photons were randomly absorbed by ABP in accordance with

Lambert's law and photoelectrons were emitted:



The secondary electrons with excess energy ionized or electronically excited ABP:



The electron trajectories after EUV absorption were calculated in accordance with the reported procedure until the electron energy was reduced to less than 21 eV.<sup>4)</sup> This threshold energy  $E_{\text{th}}$  was set so that G-value of ionization is 4.5, which was estimated using PHS.<sup>5)</sup> The inelastic mean free path of electrons  $\lambda$  (in Å) was calculated using a modified form of the Bethe equation:<sup>6)</sup>

$$\lambda = \frac{E}{\left\{ E_p^2 \left[ \beta \ln(\gamma E) - \left( \frac{C}{E} \right) + \left( \frac{D}{E^2} \right) \right] \right\}} \quad (3-4)$$

where  $E$  is the electron energy (in eV),  $E_p = 28.8(N_v \rho / M)^{1/2}$  is the free-electron plasmon energy (in eV),  $\rho$  is the density (in g cm<sup>-3</sup>),  $N_v$  is the number of valence electrons per atom (for elements) or molecule (for compounds) and  $M$  is the atomic or molecular weight;  $\beta$ ,  $\gamma$ ,  $C$ , and  $D$  are parameters. Above the threshold energy  $E_{\text{th}}$ , I assumed that the electron energy was lost by either the ionization or electronic excitation of molecules. The energy transferred to molecules upon inelastic collision was determined

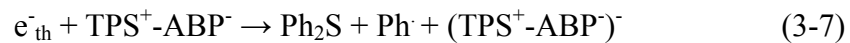
using the electron energy loss function. The ionization energy of molecules was calculated using the photoelectron emission spectrum. The angular distribution of photoelectron and secondary electron emission was not incorporated in the simulation, because the directionality of photoelectrons and secondary electrons is considered to be lost due to the multiple elastic scattering of low-energy electrons under a sub-excitational energy level.<sup>4)</sup> The inelastic mean free path,<sup>6)</sup> electron energy loss function,<sup>7)</sup> and photoabsorption spectrum<sup>8)</sup> of polymethylmethacrylate were used in the calculation mentioned above, because those of ABP are unavailable.

The low-energy electrons that are not capable of ionizing or electronically exciting molecules lose their energy by exciting intra- and intermolecular vibrational state and are finally thermalized. For the initial distribution of thermalized electrons around the generation points of secondary electrons, we have reported that an exponential function reproduced well the kinetics of subsequent reaction of intermediates in the model compounds of resist materials:<sup>9-11)</sup>

$$4\pi w_{t=0} r^2 dr = \frac{1}{r_0} \exp\left(-\frac{r}{r_0}\right) dr \quad (3-5)$$

where  $w$  and  $r_0$  represent the electron probability density and the thermalization distance (the mean initial separation distance between a thermalized electron and its parent radical cation), respectively. The values of  $r_0$  in organic compounds including polymers

have been reported to be 3-7 nm.<sup>9-13)</sup> In ABP films, the thermalized electrons migrate under the electric fields produced by other charged species until they find localization sites. The main localization sites are polymer radical cations and acid generator units. Therefore, the thermalized electrons,  $e^-_{th}$ , either recombine with polymer radical cations or react with acid generator units.<sup>14,15)</sup>



Here,  $Ph_2S$  and  $Ph\cdot$  are diphenylsulfide (DPS) and a phenyl radical, respectively. When single EUV photon was absorbed, 4.2 electrons were generated on average and were thermalized in a narrow region. The dynamics of thermalized electrons was calculated according to<sup>16)</sup>

$$\delta \mathbf{r}_i = \mu_i \mathbf{E}_i \delta t + (6D_i \delta t)^{1/2} \mathbf{R}_i \quad (3-8)$$

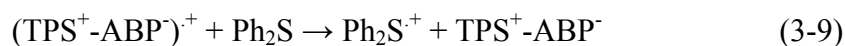
Here,  $\delta \mathbf{r}_i$  is the displacement of a charged particle during a small time step  $\delta t$ .  $\mu_i$ ,  $\mathbf{E}_i$ ,  $D_i$ , and  $\mathbf{R}_i$  are the mobility of particles, the electric field due to the Coulomb interactions with all the other particles, the diffusion coefficient and the random vector with a uniformly distributed orientation and a unit length. The mobility is related to the diffusion coefficient by  $\mu_i = eD_i/kT$  with  $e$  the charge of an electron,  $k$  the Boltzmann constant, and  $T$  the absolute temperature. The effective reaction radius for the reaction

(3-6) was set to be 0.5 nm. The reaction (3-6) is the reaction between oppositely charged species. When a thermalized electron approaches the radical cation, the thermalized electron is strongly attracted by the radical cation. Therefore, the accuracy of the value of the effective reaction radius for the reaction (3-6) does not much affect the accuracy of the simulation. The reaction of ABP with electrons has been evaluated in acetonitrile solution.<sup>17)</sup> The rate constant for the reaction of ABP with electrons in acetonitrile was  $4.0 \times 10^{10} \text{ M}^{-1} \text{ s}^{-1}$ . The rate constants for the reaction of triphenylsulfonium triflate (TPS-TF) with electrons were  $6.0 \times 10^{10} \text{ M}^{-1} \text{ s}^{-1}$ . The rate constant of ABP was two-thirds that of low-molecular-weight acid generators. However, the effective reaction radius for the reaction of thermalized electrons with ABP was assumed to be the same as that for the reaction of thermalized electrons with TPS-TF (0.7 nm),<sup>13)</sup> because the low rate constant for ABP observed in the pulse radiolysis<sup>17)</sup> is considered to be due to the low mobility of ABP. In the simulation, it was assumed that the dynamics of charged species generated by an EUV photon was not affected by the charged species generated by the other EUV photons because the measurement of quantum efficiency was carried out with the low exposure dose rate (approximately  $0.01 \text{ mJ cm}^{-2} \text{ s}^{-1}$ ). In other words, the reactions mentioned above were calculated independently for each EUV photon. When a high power exposure source is used, the calculation of the electrostatic interaction of

all the charged species will be required for the accurate estimation of the acid distribution.<sup>18)</sup>

The simulation was divided into two parts described above and below because the mobility of thermalized electrons is generally higher by two order than that of molecules. In the former part, the molecules were assumed to be immobile. With this assumption, the distribution of intermediates can be calculated without knowing the diffusion constant of thermalized electrons. The former part is basically the same as the simulation model for PHS-based resists.<sup>13)</sup> The positions of the intermediates  $[(\text{TPS}^+-\text{ABP}^-)^+, (\text{TPS}^+-\text{ABP}^-)^*, \text{Ph}_2\text{S}, \text{Ph}\cdot, (\text{TPS}^+-\text{ABP}^-)]$  were determined by calculating the electron trajectories until all the thermalized electrons were localized.

The subsequent reactions for the generation of the protons of acids are:



Here,  $\text{Ph}_2\text{S}^+$  and  $\text{Ph-Ph}_2\text{S}$  are a DPS radical cation and a phenyl-substituted DPS, respectively. DPS radical cations are generated through the hole transfer from ABP radical cation to DPS. Protons and phenyl-substituted DPS are generated through the reaction of DPS radical cations and phenyl radicals.

The reaction between phenyl radicals was taken into account because biphenyl has



been reported as a decomposition product of ABP upon exposure to  $\gamma$ -rays in the chapter 2.



Here, Ph-Ph is biphenyl. This reaction leads to the decrease of the quantum efficiency of acid generation, because the phenyl radicals required for acid generation [reaction (3-10)] are terminated.

The motion of molecules at each time step  $\delta t$  is given by  $(6D_i\delta t)^{1/2}\mathbf{R}_i$ . In the latter part of simulation, the diffusion of  $\text{Ph}_2\text{S}$ ,  $\text{Ph}_2\text{S}^+$ , and  $\text{Ph}\cdot$  was calculated. The diffusion constants of  $\text{Ph}_2\text{S}$ ,  $\text{Ph}_2\text{S}^+$ , and  $\text{Ph}\cdot$  were assumed to be inversely proportional to the molecular weight. The diffusion constant of  $\text{Ph}\cdot$  was set to be  $1 \text{ nm}^2 \text{ s}^{-1}$  for simplicity because the distribution of products does not depend on the absolute value of the diffusion constant.

The acid generation through the hole transfer to the diphenylsulfide was discussed so far. The acids are also generated through the decomposition of acid generator units from their electronic excited states, although this path is minor:



$(\text{TPS}^+-\text{ABP}^-)^*$  is generated through the reactions (3-3) and (3-6). The probability of the generation of electronically excited state in the reaction (3-6) is unknown. Because the

acid generation through this path is considered to be minor in the presence of high concentration electron scavenger (acid generator unit), the probability was assumed to be roughly 0.5. The quantum efficiency of the electronic excited state of each monomer unit and the efficiency of energy transfer between monomer units are unknown. In this simulation model, the acid generation efficiency from the electronic excited state was simply assumed to be proportional to the concentration of acid generator units. The efficiency of reaction (3-6) is, hereafter, called the acid generation efficiency from the excited states in this study.

### 3.4. Results and discussion

The acid generation in ABP films was simulated using the developed code. ABPs used for the experiments in the chapter 1 and 2 were assumed in the simulation. The molecular structure is

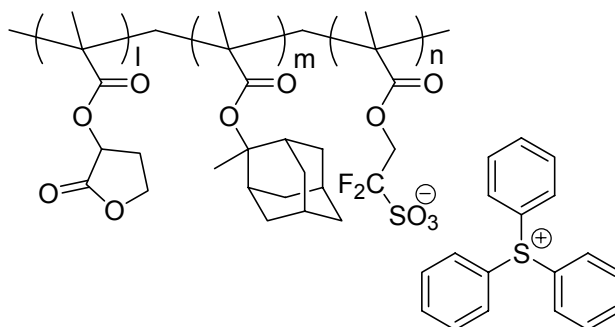


Figure 3-1. Molecular structure of anion-bound polymer.

shown in Fig. 3-1. The composition ratio of triphenylsulfonium fluoroalkylsulfonate units was changed from 5.4 to 10.9 and 14.3 mol%, which are hereafter called 5, 10, and 14 mol% ABP, respectively. Using XRD, the film densities were determined to be

1.251, 1.259, and 1.275 g cm<sup>-3</sup> for 5, 10, and 14 mol% ABP films, respectively. The concentration of acid generator units were calculated to be 0.187, 0.355, and 0.461 nm<sup>-3</sup> for 5, 10, and 14 mol% ABP films, respectively. The linear absorption coefficients of ABP films were calculated using X-Ray Form Factor, Attenuation, and Scattering Tables of NIST (National Institute of Standards and Technology).

Table 3-1. Parameters used in the simulation: <sup>\*1</sup>5 mol% ABP, <sup>\*2</sup>10 mol% ABP, and <sup>\*3</sup>14 mol% ABP.

Absorption coefficient ( $\mu\text{m}^{-1}$ )	5.45, <sup>*1</sup> 5.49, <sup>*2</sup> 5.55 <sup>*3</sup>
Resist film density ( $\text{g cm}^{-3}$ )	1.251, <sup>*1</sup> 1.259, <sup>*2</sup> 1.275 <sup>*3</sup>
Dielectric constant	4.05, <sup>*1</sup> 4.20, <sup>*2</sup> 4.57 <sup>*3</sup>
Acid generator concentration (mol%)	5.4, <sup>*1</sup> 10.9, <sup>*2</sup> 14.3 <sup>*3</sup>
Exposure dose ( $\text{mJ cm}^{-2}$ )	3.86, <sup>*1</sup> 7.73, <sup>*2</sup> 11.6 <sup>*3</sup>
Thermalization distance (nm)	3-7
$\rho$ ( $\text{g cm}^{-3}$ ) <sup>6)</sup>	1.19
$N_v$ <sup>6)</sup>	40
$M$ <sup>6)</sup>	100.1
$\beta$ <sup>6)</sup>	0.0152
$\gamma$ <sup>6)</sup>	0.155
$C$ <sup>6)</sup>	1.15
$D$ <sup>6)</sup>	21
Effective reaction radius of reactions (3-6) and (3-7) (nm) <sup>11)</sup>	0.7
Effective reaction radius of reaction (3-9) (nm)	0.5
Effective reaction radius of reaction (3-10) (nm)	0.5
Ratio of $(\text{TPS}^+-\text{ABP}^-)^*$ and $\text{TPS}^+-\text{ABP}^-$ of reaction (3-6)	0.5

The linear absorption coefficient of 5, 10, and 14 mol% ABP films were 5.45, 5.49, and  $5.55 \mu\text{m}^{-1}$ , respectively. Using SSM 600 CV, the dielectric constants of 5, 10, and 14 mol% ABP films were determined to be 4.05, 4.20 and 4.57, respectively. The exposure doses were set to be the same values as those used in the experiments for the evaluation of the quantum efficiencies of acid generation, namely, 3.86, 7.73, and  $11.6 \text{ mJ cm}^{-2}$ . The

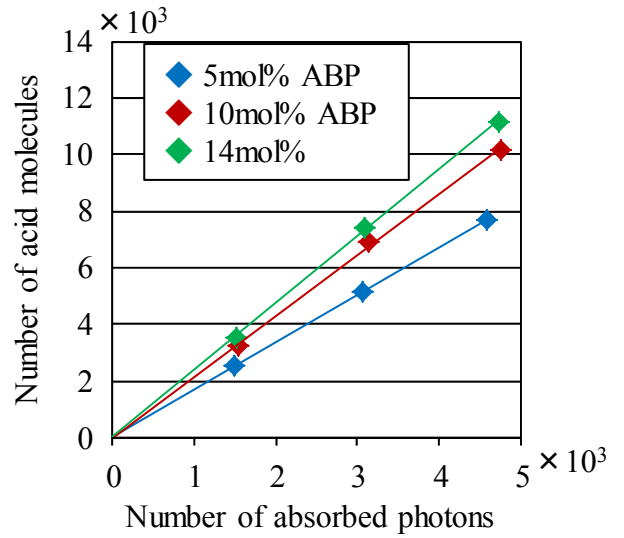


Figure 3-2. Representative relationship between the numbers of absorbed photons and acids generated in the target volume ( $50 \times 50 \times 50 \text{ nm}^3$ ). The corresponding exposure doses were 3.86, 7.73, and  $11.6 \text{ mJ cm}^{-2}$ .  $r_0$ ,  $R_B$ ,  $\epsilon_E(5)$ ,  $\epsilon_E(10)$ , and  $\epsilon_E(14)$  were 3 nm, 0.20 nm, 0.30, 0.57, and 0.74, respectively.

parameters used in the simulation were summarized in Table 3-1. Figure 3-2 shows the representative relationship between the numbers of absorbed photons and acids generated in the target volume. The quantum efficiency of acid generation was determined from the slope of the graph, similarly to the experiments for the evaluation of quantum efficiency. The quantum efficiencies of 5, 10, and 14 mol% ABP films were 1.69, 2.16, and 2.36, respectively. Similarly, the quantum efficiency was calculated by changing the thermalization distance of secondary electrons  $r_0$ , the effective reaction radius for the reaction between phenyl radicals  $R_B$ , and the acid generation efficiency

from the excited states  $\varepsilon_E$ . Hereafter,  $\varepsilon_E$  of 5, 10, and 14 mol% ABP films is expressed as  $\varepsilon_E(5)$ ,  $\varepsilon_E(10)$ , and  $\varepsilon_E(14)$ , respectively.

The quantum efficiency of acid generation was calculated for  $r_0=3$  nm. Figures 3-3(a)-(c) show the dependence of quantum efficiency on  $R_B$  and  $\varepsilon_E$ . The quantum efficiency decreased with the increase of  $R_B$  and increased with the increase of  $\varepsilon_E$ . The straight lines in Figs. 3-3(a)-(c) represent the experimental quantum efficiencies. The experimental error is approximately 10%. The deviation between experimental and calculated quantum efficiencies (fitting error) is plotted for each parameter set ( $R_B$  and  $\varepsilon_E(5)$ ) in Figs. 3-3(d) and (e). The calculated quantum efficiencies agreed with experimental data within the error of 10% for  $R_B$  range of 0.20-0.35 and for  $\varepsilon_E(5)$  range of 0.3-0.5. In the simulation, the effective reaction radius for the reaction of phenyl radicals with DPS radical cations was assumed to be 0.5 nm as mentioned before. The estimated range of  $R_B$  indicated that the reactivity of phenyl radicals with phenyl radicals is slightly lower than that with DPS radical cations. This result is reasonable, considering the difference in their molecular sizes. Within the estimated range of  $R_B$  (0.20-0.35), the corresponding  $\varepsilon_E(5)$  increased with  $R_B$ .

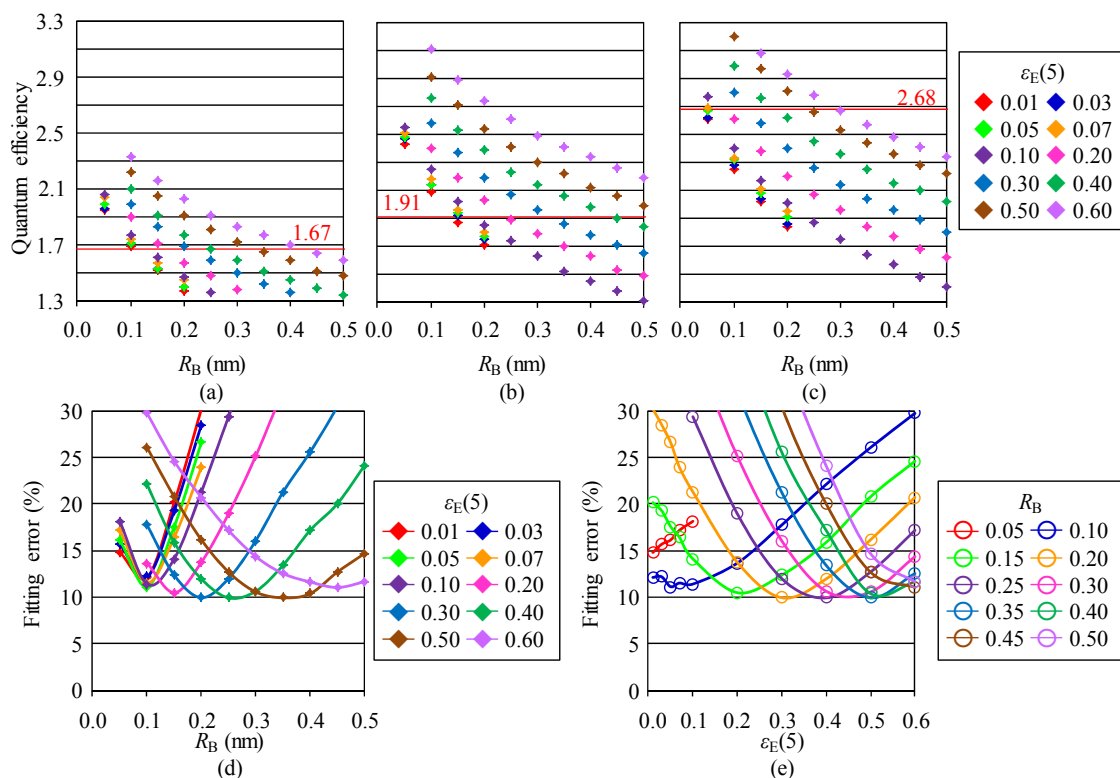


Figure 3-3. Dependence of quantum efficiency on  $R_B$  and  $\varepsilon_E(5)$  for  $r_0=3$  nm: (a) 5, (b) 10, and (c) 14 mol% ABP. The horizontal straight lines and numerical values in (a)-(c) represent the experimental quantum efficiencies. (d) and (e) are the deviation between experimental and calculated quantum efficiencies (fitting error).

Because  $R_B$  indicates the efficiency of the deactivation of phenyl radicals, the increase of  $R_B$  means the decrease of the yield of acids generated through the reactions (3-9) and (3-10). The decreased yield was compensated for by increasing  $\varepsilon_E$  in the fitting procedure. The quantum efficiency of acid generation upon exposure to DUV and VUV light has been reported to be 0.05-0.63.<sup>19,20)</sup>  $\varepsilon_E$  includes the efficiency of energy transfer. Therefore,  $\varepsilon_E$  is considered to be less than the quantum efficiency of acid generation upon exposure to DUV and VUV light. The estimated range of  $\varepsilon_E(5)$  seems reasonable.

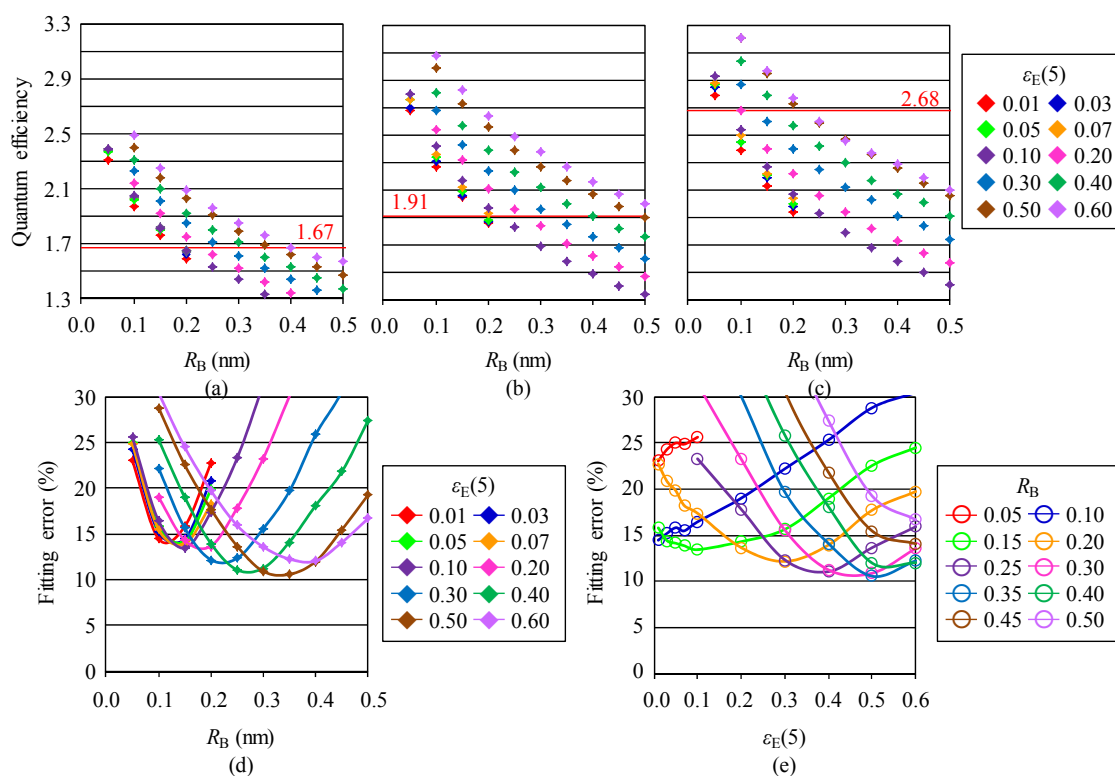


Figure 3-4. Dependence of quantum efficiency on  $R_B$  and  $\epsilon_E(5)$  for  $r_0=6$  nm: (a) 5, (b) 10, and (c) 14 mol% ABP. The horizontal straight lines and numerical values in (a)-(c) represent the experimental quantum efficiencies. (d) and (e) are the deviation between experimental and calculated quantum efficiencies (fitting error).

However, the corresponding ranges of  $\epsilon_E(10)$  and  $\epsilon_E(14)$  were 0.57-0.95 and 0.74-1.00, respectively, owing to the reason discussed in the section 3. Therefore, the most probable parameter set ( $R_B$  and  $\epsilon_E(5)$ ) is (0.20, 0.3). The thermalization distance in resist model compounds has been reported to be 3-7 nm.<sup>9-11)</sup> The thermalization distance in model polymers for resist materials has been also investigated and estimated to be 3.2 nm for PHS<sup>13)</sup> and 6 nm for polymethylmethacrylate.<sup>12)</sup> Assuming  $r_0=6$  nm, the similar calculation was carried out as shown in Fig. 3-4. When the same parameter set ( $R_B$  and

$\epsilon_E$ ) as that for  $r_0=3$  nm was assumed, the quantum efficiency slightly increased by increasing  $r_0$  from 3 to 6 nm. This is because the probability that the thermalized electrons encounter the acid generator units increased with the increase of thermalization distance. The dependence of quantum efficiency on  $R_B$  and  $\epsilon_E(5)$  showed the same trend as the case for  $r_0=3$  nm. The deviation between experimental and calculated quantum efficiencies is plotted for each parameter set ( $R_B$  and  $\epsilon_E(5)$ ) in Figs. 3-4(d) and (e). The fitting error slightly increased and the error minimum became clear, compared with the case for  $r_0=3$  nm. The best fit parameter set was ( $R_B, \epsilon_E(5)$ )=(0.35, 0.5). Similarly to the case for  $r_0=3$  nm, the reactivity of phenyl radicals with phenyl radicals was slightly lower than that with DPS radical cations. As discussed above,  $\epsilon_E$  includes the efficiency of energy transfer. Because  $\epsilon_E(14)$  is 1.0 under the assumption of this study when  $\epsilon_E(5)$  is 0.5, this parameter set is unlikely. Although the possibility of  $r_0=6$  nm cannot be denied,  $r_0=3$  nm is more probable than  $r_0=6$  nm. The diffusion lengths of DPS and phenyl radicals were calculated with the parameter set ( $R_B$  and  $\epsilon_E$ ) best-fitted to the experimental quantum efficiencies for each thermalization distance.



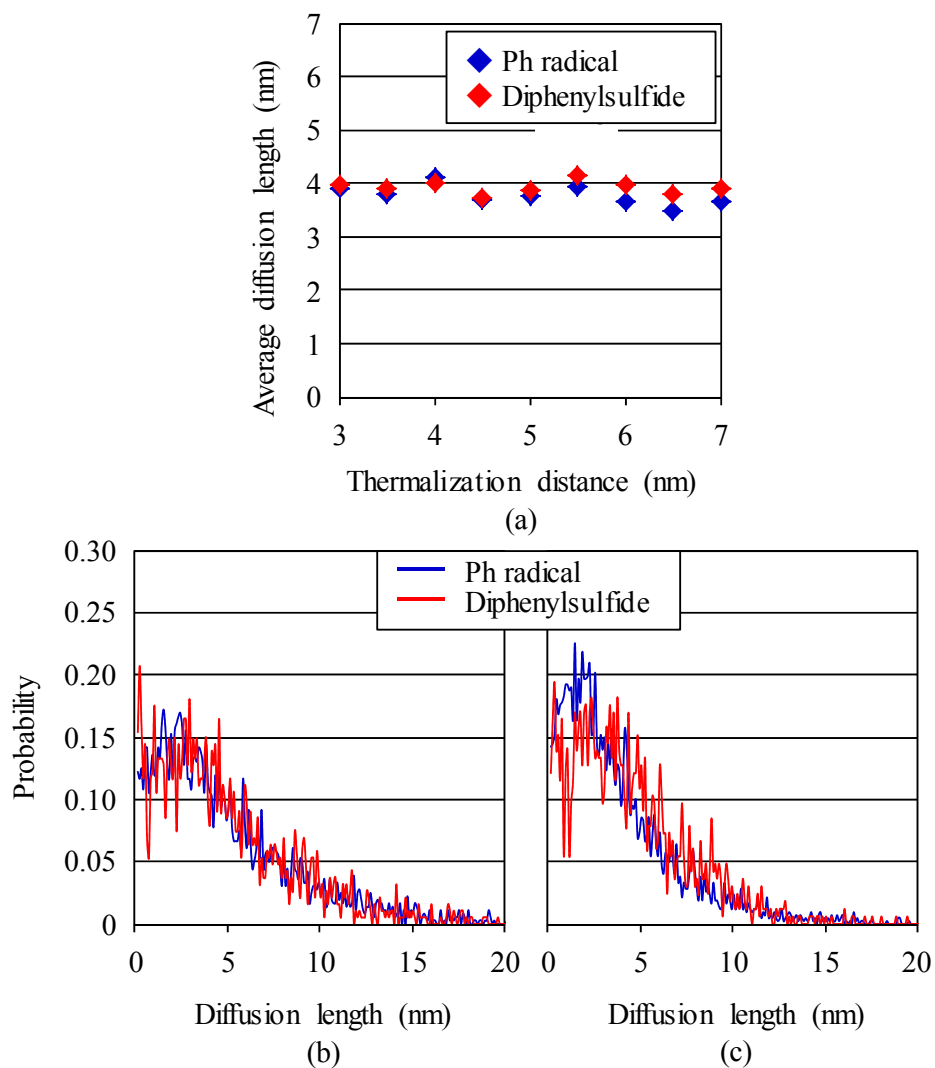


Figure 3-5. (a) Average diffusion length of DPS before the reaction with phenyl radicals and that of phenyl radicals before the reaction with DPS radical cations or phenyl radicals, calculated with the best-fit parameter set ( $R_B$  and  $\epsilon_E$ ) for each thermalization distance. (b) Probability of each diffusion length, calculated with the best-fit parameter set ( $R_B$ ,  $\epsilon_E(5)$ )=(0.20, 0.3) for  $r_0=3$  nm. (c) Probability of each diffusion length, calculated with the best-fit parameter set ( $R_B$ ,  $\epsilon_E(5)$ )=(0.35, 0.5) for  $r_0=6$  nm.

Figure 3-5(a) shows the average diffusion length of DPS before the reaction with phenyl radicals and that of phenyl radicals before the reaction with DPS radical cations or

phenyl radicals. The average diffusion length of DPS and phenyl radicals did not significantly depend on the thermalization distance and was approximately 4 nm. The probability of each diffusion length is plotted in Figs.

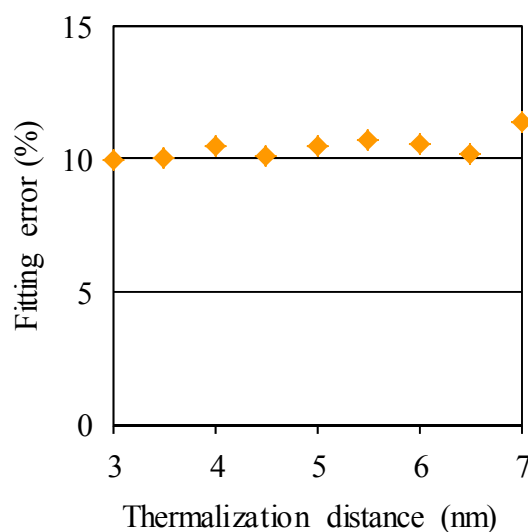


Figure 3-6. Fitting errors minimized for each thermalization distance.

3-5(b) and (c). There was not a significant difference between the

distributions of diffusion lengths of DPS and phenyl radicals. Also, there was not a significant difference between the distributions of diffusion lengths for  $r_0=3$  and 6 nm.

It has been reported that benzene is one of main outgas components during exposure to EUV.<sup>21-23)</sup> Therefore, the diffusion of phenyl radicals is possible. However, the diffusion of DPS should be discussed. The 10-nm diffusion of DPS in solid films, as shown in Fig. 3-5, may not be possible. Although the hole was assumed to be immobile except for the hole transfer between ABP radical cations and DPS in the proposed simulation model, the hole migration along with the polymer chain and/or between polymer molecules may have contributed to the generation of DPS radical cations and then the generation of protons in the real resists. In such case, both DPS diffusion and hole migration are

considered to contribute to the acid generation in anion-bound chemically amplified resists. Within the plausible thermalization distance range, the fitting errors are plotted for each thermalization distance in Fig. 3-6. With the decrease of thermalization distance, the fitting error decreased. Because the decrease of fitting error was little, we cannot determine the thermalization distance from the fitting error alone. Considering the discussion regarding Figs. 3-3 and 3-4, the thermalization distance of 3 nm is the most probable among the examined thermalization distances.

Figure 3-7 shows the distribution of the protons and anions of acids around the absorption point of EUV photons (the origin of the graph), expressed in the form of probability line density. Here, the anions mean the anion units, the cation parts of which were decomposed by the exposure to EUV. The integral of the graph (area) corresponds to the quantum efficiency. The distribution of the protons generated through the dissociative electron attachment and the distribution of the protons generated from the electronic excited state of acid generator units are also shown in Fig. 3-7. The distribution of protons did not correspond to that of anions. The difference in the areas means the difference in their quantum efficiency.

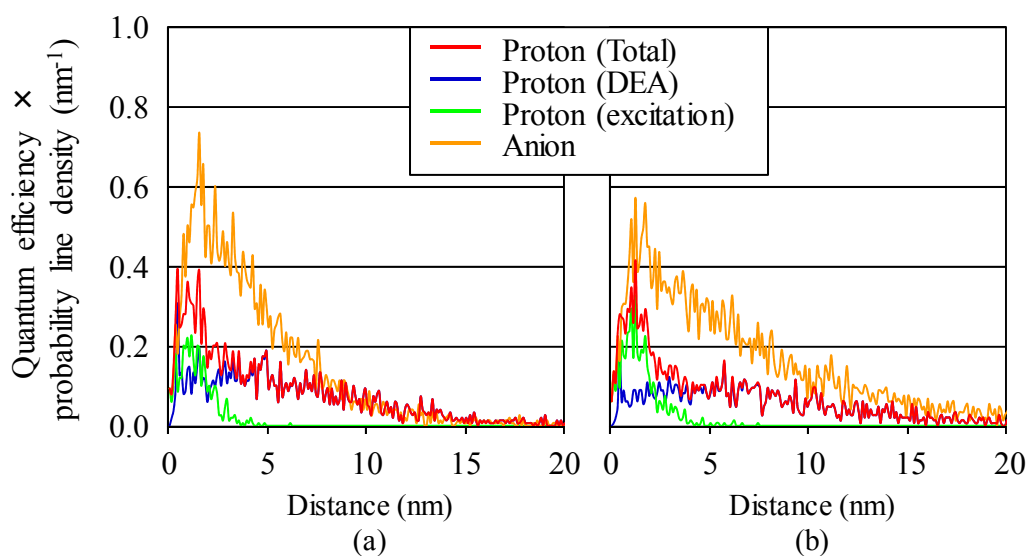


Figure 3-7. Distribution of the protons and anions of acids around the absorption point of EUV photons. (a) Distribution calculated with the best-fit parameter set  $(R_B, \varepsilon_E(5)) = (0.20, 0.3)$  for  $r_0=3$  nm. (b) Distribution calculated with the best-fit parameter set  $(R_B, \varepsilon_E(5)) = (0.35, 0.5)$  for  $r_0=6$  nm. The distribution marked by “DEA” is the distribution of the protons generated through the dissociative electron attachment. The distribution marked by “excitation” is the distribution of the protons generated from the electronic excited state of acid generator units. The absorption point of EUV photons is the origin of the graph. The vertical axis represents the product of quantum efficiency and probability line density per spherical shell thickness (nm). The integral of the graph (area) corresponds to the quantum efficiency.

The area of proton distribution is less than that of anions. This is because some holes generated through ionization were not converted to protons and remain cations such as DPS radical cations. The average distances of protons from the absorption points of photons for  $r_0=3$  and 6 nm were 4.56 and 6.12 nm, respectively. Also, the average distance of protons from the absorption points of photons for  $r_0=7$  nm was 6.33 nm. Therefore, the blur of proton distribution intrinsic to the reaction mechanisms of

anion-bound chemically amplified resists is roughly 4.5-6.5 nm.

### **3-5. Summary**

The acid generation processes in the anion-bound chemically amplified resists upon exposure to EUV radiation were modeled for the development of a Monte Carlo simulation code. Using the developed simulation code, the dependence of the quantum efficiency of acid generation on the concentration of acid generator units was calculated. The experimental quantum efficiencies were well reproduced, within the thermalization distance range of 3-7 nm. The thermalization distance of 3 nm is considered to be the most probable. At the thermalization distance of 3 nm, the best-fit  $R_B$  and  $\epsilon_E(5)$  were 0.20-0.35 nm and 0.3-0.5, respectively. The blur of proton distribution intrinsic to the reaction mechanisms of anion-bound chemically amplified resists was estimated to be roughly 4.5-6.5 nm.

## References

- 1) T. Itani and T. Kozawa, *Jpn. J. Appl. Phys.* **52**, (2013) 010002.
- 2) J. L. Dektar and N. P. Hacker, *J. Am. Chem. Soc.* **112**, (1990) 6004.
- 3) T. Kozawa and S. Tagawa, *Jpn. J. Appl. Phys.* **49**, (2010) 030001.
- 4) T. Kozawa, S. Tagawa, H. B. Cao, H. Deng, and M. J. Leeson, *J. Vac. Sci. Technol. B* **25**, (2007) 2481.
- 5) T. Kozawa, T. Shigaki, K. Okamoto, A. Saeki, S. Tagawa, T. Kai, and T. Shimokawa, *J. Vac. Sci. Technol. B* **24**, (2006) 3055.
- 6) S. Tanuma, C. J. Powell, and D. R. Penn, *Surf. Interface Anal.* **21**, (1993) 165.
- 7) P. D. Vera, I. Abril, and R. Garcia-Molina, *J. Appl. Phys.* **109**, (2011) 094901.
- 8) K. K. Okudaira, S. Hasegawa, P. T. Sprunger, E. Morikawa, and V. Saile, *J. Appl. Phys.* **83**, (1998) 4292.
- 9) A. Saeki, T. Kozawa, Y. Yoshida, and S. Tagawa, *Jpn. J. Appl. Phys.* **41**, (2002) 4213.
- 10) K. Okamoto, T. Kozawa, M. Miki, Y. Yoshida, and S. Tagawa, *Chem. Phys. Lett.* **426**, (2006) 306.
- 11) K. Okamoto, T. Kozawa, A. Saeki, Y. Yoshida, and S. Tagawa, *Radiat. Phys. Chem.* **76**, (2007) 818.
- 12) T. Kozawa, S. Tagawa, T. Kai, and T. Shimokawa, *J. Photopolym. Sci. Technol.* **20**, (2007) 577.
- 13) T. Kozawa and S. Tagawa, *Jpn. J. Appl. Phys.* **50**, (2011) 030209.
- 14) T. Kozawa, Y. Yoshida, M. Uesaka, and S. Tagawa, *Jpn. J. Appl. Phys.* **31**, (1992)

- 4301.
- 15) K. Natsuda, T. Kozawa, K. Okamoto, A. Saeki, and S. Tagawa, *Jpn. J. Appl. Phys.* **48**, (2009) 06FC05.
  - 16) W. M. Bartczak and A. Hummel, *J. Chem. Phys.* **87**, (1987) 5222.
  - 17) S. Enomoto, D. T. Nguyen, and S. Tagawa, *Jpn. J. Appl. Phys.* **52**, (2013) 06GC03.
  - 18) K. Okamoto, T. Kozawa, K. Oikawa, T. Hatsui, M. Nagasono, T. Kameshima, T. Togashi, K. Tono, M. Yabashi, H. Kimura, Y. Senba, H. Ohashi, R. Fujiyoshi, and T. Sumiyoshi, *Appl. Phys. Express* **5**, (2012) 096701
  - 19) J. F. Cameron, N. Chan, K. Moore, and G. Pohlers, *Proc. SPIE* **4345**, (2001) 106.
  - 20) D. R. Mckean, U. P. Schaedeli, P. H. Kasai, and S. A. Macdonald, *J. Polym. Sci., Part A. Polym Chem.* **29**, (1991) 309.
  - 21) H. Oizumi, K. Matsumaro, J. Santillan, and T. Itani, *Proc. SPIE* **7636**, (2010) 106.
  - 22) K. R. Dean, K. E. Gonsalves, and M. Thiyagarajan, *Proc. SPIE* **6153**, (2006) 61531E.
  - 23) I. Pollentier, *J. Photopolym. Sci. Technol.* **5**, (2010) 605.

## Conclusion

In this thesis, the reaction mechanism induced by ionizing radiation in anion-bound polymer was elucidated using electron (pulse),  $\gamma$ , and EUV radiolysis and simulation. A simulation code was developed based on the elucidated reaction mechanism. Using the developed simulation code, the dependence of the quantum efficiency of acid generation on the concentration of acid generator units was calculated. The experimental quantum efficiencies were well reproduced. The results in each chapter of this thesis are summarized as follows.

In chapter 1, the electron and hole transfer induced in the anion-bound polymer solution in CH was investigated. The electron was transferred to the anion-bound polymer. The hole was captured by diphenylsulfide, which is a decomposition product of the anion-bound polymer and a non-proton source. It was confirmed that the formation of the radical cation of diphenylsulfide is suppressed in the presence of a well-known proton source for resist materials (phenol).

In chapter 2, the radiation chemistry induced in the anion-bound polymer films was investigated using  $\gamma$  and EUV radiolysis. On the basis of experimental results, the acid generation mechanism in anion-bound chemically amplified resists was proposed. In ABP films, ABP radical cations and electrons are generated through ionization upon



exposure to ionizing radiations such as EUV. ABP reacts with electrons to produce DPS and phenyl radicals through the dissociative electron attachment. DPS radical cations are generated through the hole transfer from ABP radical cation to DPS. The major path for the proton generation in the absence of effective proton sources is considered to be the reaction of phenyl radicals with DPS radical cations.

In chapter 3, the acid generation processes in the anion-bound chemically amplified resists upon exposure to EUV radiation were modeled for the development of a Monte Carlo simulation code. Using the developed simulation code, the dependence of the quantum efficiency of acid generation on the concentration of acid generator units was calculated. The experimental quantum efficiencies were well reproduced

## List of Publication

The contents of this thesis are composed of the following papers.

- 1) Electron and Hole Transfer in Anion-Bound Chemically Amplified Resists Used in Extreme Ultraviolet Lithography

Yoshitaka Komuro, Hiroki Yamamoto, Yoshiyuki Utsumi, Katsumi Ohomori,  
and Takahiro Kozawa

Applied Physics Express, 2013, 6, 014001-1- 014001-4

- 2) Acid generation mechanism in anion-bound chemically amplified resists used for extreme ultraviolet lithography

Yoshitaka Komuro, Hiroki Yamamoto, Kazuo Kobayashi, Yoshiyuki Utsumi,  
Katsumi Ohomori, and Takahiro Kozawa

Japanese Journal of Applied Physics, 2014, 53, 116503-1-116503-8

- 3) Modeling and simulation of acid generation in anion-bound chemically amplified resists used for extreme ultraviolet lithography

Yoshitaka Komuro, Daisuke Kawana, Taku Hirayama, Katsumi Ohomori, and  
Takahiro Kozawa

Published in Japanese Journal of Applied Physics, 2015, 54.

## **Acknowledgment**

The studies described in this dissertation have been carried out under the direction of Professor Takahiro Kozawa at the Department of Beam Material Science, Graduate School of Engineering, The Institute of Scientific and Industrial Research Osaka University during 2012-2015.

I wish to express my gratitude to Professor Takahiro Kozawa for his continuous guidance and invaluable suggestions.

I also wish to express my gratitude to Professor Toshikazu Hirao and Professor Yoichi Ando for his sincere guidance.

I am sincerely grateful to Associate Professor Yusa Muroya at the Kozawa research group.

I am sincerely grateful to Assistant Professor Hiroki Yamamoto and Kazuo Kobayashi at the Kozawa research group.

I also wish to thank all members of Kozawa laboratory for their useful advice and discussion.; Dr. Mayu Fujikawa, Mr. Tomoharu Yamazaki, Mr. Daisuke Hatamoto, Mr. Masaki Mitsuyasu, Mr. Akihiro Konda, Mr. Tetsuro Yoshida, Mrs. Kinuko Watanabe.

I express warm thanks to Katsumi Ohmori of TOKYO OHKA KOGYO Corporation for constant encouragement. It would not have been possible to start my engineering career and entry into graduate school of engineering without his guidance.

I am grateful to Taku Hirayama and Daisuke Kawana of TOKYO OHKA KOGYO Corporation for constant encouragement, aspiring guidance and technically constructive discussion.

I am grateful to Yoshiyuki Utsumi for teaching me the correct way to identify and solve problems. It would not have been possible to start my engineering career without his heartfelt guidance on experimental science.

The completion of this thesis would not have been possible either without the expertise of all the staff at the Research and Development Department , New Business Development Department, and Inspection Department at TOKYO OHKA KOGYO Corporation. To F. Kaneko, R. Takasu, H. Shimizu, S. Hidesaka, R. Uchida, A. Kawaue, T. Seshimo, T Dazai, K. Matsuzawa, M. Arai, T. Maehashi, H. Yamazaki, I. Suzuki, K. Miyagi, D. Shiono, I. Takagi, S. Matumaru, T. Matumiya, T. Kurosawa, K. Suzuki, T.

Kamizono, T. Fujii, M. Yahagi, H. Yamano, M. Shinomiya, T. Hirano, T. Kaiho, T.

Nagamine, Y. Hori, T. Hato, J. Tsuchiya, M. Irie, A. Momozawa, S. Katayama, Y.

Yamamoto, Y. Taira, C. Shinohara, T. Mimura, T. Nakata, C. Harada, M. Miwa, T.

Tachikawa, Y. Matsuda, T. Haga, A. Goshima, K. Kobayashi, K. Dohtani, K. Yamada, S.

Sasaki, K Shimotori. I am grateful for everything they have done for me.

I would like to acknowledge H. Sato, K. Sato, K. Wakiya, H. Komano, J. Onodera, M. Yoshizaki, A. Yamazaki, A. Sawano, M. Shida, S. Fujimura, S. Asahi of TOKYO OHKA KOGYO Corporation for their continuous encouragement throughout the thesis project.

Finally, I thank my parents, Yoichi and Fumie Komuro; my Sister, Erina Komuro for their love throughout my doctoral research.